Formation and growth of sub-3-nm aerosol particles in experimental chambers

Dada, Lubna

2020-03

Dada , L , Lehtipalo , K , Kontkanen , J , Nieminen , T , Baalbaki , R , Ahonen , L , Duplissy , J , Yan , C , Chu , B , Petäjä , T , Lehtinen , K , Kerminen , V-M , Kulmala , M & Kangasluoma , J 2020 , ' Formation and growth of sub-3-nm aerosol particles in þÿ e x p e r i m e n t a l   c h a m b e r s ' ,   N a t u r e   P r o t o c o l s ,   v o l .   1 5 ,   n o .   3 ,   p p .   1 0 1 3

http://hdl.handle.net/10138/318908
https://doi.org/10.1038/s41596-019-0274-z

acceptedVersion

nature protocols

PROTOCOL

https://doi.org/10.1038/s41596-019-0274-z

Formation and growth of sub-3-nm aerosol particles in experimental chambers

Lubna Dada[1], Katrianne Lehtipalo[1,2], Jenni Kontkanen[1], Tuomo Nieminen[1], Rima Baalbaki[1], Lauri Ahonen[1], Jonathan Duplissy[1,3], Chao Yan[1,4], Biwu Chu[1], Tuukka Petäjä[1,5], Kari Lehtinen[6,7], Veli-Matti Kerminen[1], Markku Kulmala[1,4*] and Juha Kangasluoma[1,4*]

Atmospheric new particle formation (NPF), which is observed in many environments globally, is an important source of boundary-layer aerosol particles and cloud condensation nuclei, which affect both the climate and human health. To better understand the mechanisms behind NPF, chamber experiments can be used to simulate this phenomenon under well-controlled conditions. Recent advancements in instrumentation have made it possible to directly detect the first steps of NPF of molecular clusters (~1–2 nm in diameter) and to calculate quantities such as the formation and growth rates of these clusters. Whereas previous studies reported particle formation rates as the flux of particles across a specified particle diameter or calculated them from measurements of larger particle sizes, this protocol outlines methods to directly quantify particle dynamics for cluster sizes. Here, we describe the instrumentation and analysis methods needed to quantify particle dynamics during NPF of sub-3-nm aerosol particles in chamber experiments. The methods described in this protocol can be used to make results from different chamber experiments comparable. The experimental setup, collection and post-processing of the data, and thus completion of this protocol, take from months up to years, depending on the chamber facility, experimental plan and level of expertise. Use of this protocol requires engineering capabilities and expertise in data analysis.

Introduction

New particle formation (NPF) is a major source of atmospheric aerosol particles[1,2]. It contributes substantially to global cloud condensation nuclei concentrations[3,4] and may also contribute to haze formation[5]. NPF involves the formation of sub-3-nm charged and neutral clusters from atmospheric vapors and their growth to stable aerosol particles[6–8]. This phenomenon is observed in a wide range of environments with varying levels of precursor vapors and different meteorological conditions[9,10]. The mechanisms leading to cluster formation and subsequent growth are currently under investigation, as are the particle-formation potentials of different biogenic and anthropogenic precursor vapors and their relative importance. However, studying these processes on the basis of field measurements is challenging because the contributions of different factors cannot be isolated and studied independently. There is also a lack of reliable atmospheric observations from many environments because of difficulties in operating all the necessary instrumentation under challenging field conditions. Consequently, scientists studying NPF have relied on laboratory experiments to validate their hypotheses, unveil hidden mechanisms and make new discoveries.

Development of the protocol

In general, chambers have been operated to evaluate atmospheric gas-phase chemical mechanisms governing particle formation and to characterize secondary organic aerosols (SOAs)[11–49]. However, older laboratory measurements were often hampered by unmeasured contaminant levels, atmospherically irrelevant high vapor concentrations and insufficient instrumentation to detect the forming clusters and their precursors[50–53]. In addition, all these studies relied on detection of particles >3 nm. More recent laboratory experiments have allowed for highly controlled experimental

[1]Institute for Atmospheric and Earth System Research/Physics, Faculty of Science, University of Helsinki, Helsinki, Finland. [2]Atmospheric Composition Research, Finnish Meteorological Institute, Helsinki, Finland. [3]Helsinki Institute of Physics, University of Helsinki, Helsinki, Finland. [4]Aerosol and Haze Laboratory, Beijing Advanced Innovation Center for Soft Matter Science and Engineering, Beijing University of Chemical Technology, Beijing, China. [5]Joint International Research Laboratory of Atmospheric and Earth System Sciences, Nanjing University, Nanjing, China. [6]Department of Applied Physics, University of Eastern Finland, Kuopio, Finland. [7]Atmospheric Research Centre of Eastern Finland, Finnish Meteorological Institute, Kuopio, Finland. *e-mail: markku.kulmala@helsinki.fi; juha.kangasluoma@helsinki.fi

conditions (in terms of precursor concentrations and external conditions such as temperature and humidity) for studying the basic physical and chemical mechanisms behind particle formation and growth at a molecular level[23,54–101]. These experiments were also used for imitating different present-day[34,102] or preindustrial environments[103–105], as well as for making projections into the future by screening changes induced by air pollution mitigation and global warming. Scientists have even simulated clouds on other planets, such as Mars[106]. In experimental reactors, it is usually possible to change one variable at a time to study its effects on particle properties and formation and growth mechanisms. Laboratory experiments can also be repeated under constant meteorological conditions, unlike atmospheric observations.

Collectively, chambers and flow tubes are referred to as environmental reactors. Flow tubes are tubular; the reactants are introduced at one end into the mixing area, and the products are sampled from the other end for analysis[107]. A chamber usually has a higher volume-to-surface ratio than do flow tubes, which minimizes the wall loss effect described in the following sections[108]. In addition, chambers have a vertical orientation, in contrast to flow tubes, which results in smaller particle losses[109]. Reactants are mixed actively (using a fan) or passively into the whole chamber volume before sample collection. Chambers also enable collection of higher sample volumes than do flow tubes. Chambers can be operated in either batch or continuous mode. In batch mode, the reactants are introduced into the chamber, left to react and then sampled for analysis. Chambers with flexible walls are more suitable for such experiments. In continuous mode, a constant flow of synthetic air (or a similar gaseous mixture) is introduced into the reactor in order to maintain a steady pressure to compensate for the flow rate of the sampling instruments. In continuous mode, concentrations of reactants eventually reach a steady state. The chambers operated in continuous mode are known as continuously mixed flow reactors (CMFRs) regardless of whether reactants are actively mixed or not[110]. Flow tubes are discussed further in the 'Chamber considerations and requirements' section, but this protocol focuses on the use of experimental chambers.

The chemical systems that have been studied in experimental flow reactors vary between simple binary acid–water systems and more complex systems involving several precursor vapors and oxidants. Sulfuric acid binary nucleation with water has been the focus of the vast majority of NPF experiments[51,52,59–65,67,69,73,83,111]. Other studies concentrated on the ternary nucleation of sulfuric acid–water with ammonia[52,64,71,73] or amines[52,64,71–73,76,78,81], and aromatic vapors[58]. A small number of studies have focused on methane sulfonic acid (MSA) nucleation[79,80,84]. Similar chemical systems involving sulfuric acid have also been studied in chambers[54,58,74,75,82,90,95,96,102]. Recently, many chamber experiments have studied NPF involving organic compounds, such as monoterpenes, sesquiterpenes and isoprene[23,70,75,85,87,89,94,95,97,98,102,112]. Some chamber studies used emissions from real plants or trees[86,91,113]. A large number of other chamber and flow tube studies have concentrated on particle mass yields and formation of secondary organic aerosols, but they are out of the scope of this protocol.

The procedure described in this protocol has been used by Wagner et al.[97] and Lehtipalo et al.[102] for obtaining particle formation rates (J_{dp} values) and growth rates (GRs) from experiments in the CLOUD (cosmics leaving outdoor droplets) chamber (Table 1), and it builds upon the earlier NPF studies by the CLOUD collaboration[54,74,77,96,98,103], as well as experience from earlier laboratory and field studies. Many methods have been proposed to quantify NPF, and these could potentially yield different results from the same dataset. Similar to the protocol for analyzing J_{dp} and GR from atmospheric data presented by Kulmala et al.[114], we describe in this protocol a standard procedure for acquiring particle dynamics from chamber measurements.

In earlier chamber studies[77,98,102], the error on the J_{dp} values was calculated on the basis of the propagation of error, by taking into account the statistical and systematic uncertainties and run-to-run repeatability in the chamber (assumed to be 30% for the CLOUD chamber). The systematic errors include errors in the concentration measurement, dilution and wall loss, whereas the statistical errors include uncertainty in dN/dt (time-derivative of the total particle concentration above a certain threshold) and coagulation sink. In this protocol, in addition to analyzing J_{dp} and GR values from chamber experiments, we present a recommended method for calculating the error in their measurement.

Overview of the procedure

In this protocol, we introduce a standard method for measuring, correcting and analyzing particle formation dynamics from chamber experiments in order to make results from different chamber experiments comparable. With the advancement of particle counters and mass spectrometers,

Table 1 | Abbreviations

D	Diffusion coefficient
d_p	Mobility diameter of particle
$d_{p,mean,i}$	Mean diameter of the size bin i
$d_{p,ref}$	Mobility diameter of the reference particle
d_u	Upper diameter of size bin
F	Experimentally determined correction factor for wall loss in chamber
GR	Particle growth rate
J	Formation rate
J_{ap}	Apparent formation rate
J_{dp}	Formation rate of particles with diameter d_p
$J^{\pm}_{dp}$	Formation rate of ions (charged particles) with diameter d_p
J_n	Formation rate of neutral particles
$J_{n,tot}$	Neutral fraction of the total formation rate
J_{rec}	Formation rate of neutral particles by recombination of ions
J_{tot}	Total particle formation rate
$K(d_p,d_p')$	Coagulation coefficient between particles of d_p and d_p' sizes
k_{coag}	Coagulation coefficient
k_{dil}	Dilution coefficient specific for a specific chamber volume and total flow
$k_{wall}(d_p,t)$	Wall-loss coefficient of particles with diameter d_p at time t
N	Particle number concentration
N_{dp}	Particle number concentration of particles with diameter d_p
$N_{>dp}$	Particle number concentration above a certain diameter
$N^{\pm}_{<dp}$	Charged particle number concentration of charged particles with smaller than d_p
$N^{\pm}_{dp-du}$	Charged particle number concentration in size bin of diameters (d_p) and upper diameter (d_u)
$N_{dpi-dpi+1}$	Particle number concentration in a size bin
$n(d_p,t)$	Number distribution of particles with diameter d_p at time t
$N(t)$	Number concentration of particles at time t
$Q(d_p,t)$	Source term for particle with diameter d_p at time t
$S(d_p,t)$	Sink terms for particle with diameter d_p at time t
S_{att}	Production rate of ions by ion–neutral attachment
S_{coag}	Coagulation loss rate in the chamber
S_{dil}	Dilution loss rate
S_{growth}	Loss rate of ions due to growth out of the size bin
S_{rec}	Ion–ion recombination loss rate
S_{wall}	Diffusional loss rate to the chamber walls
T	Temperature
T_{ref}	Reference temperature
t	Time
t_0	Time at the beginning of the experiment
$t_{app,i}$	Time when concentration of size bin i starts to rise
$t_{app50,i}$	Time when the concentration in size bin i reaches 50% of its maximum
t_{max}	Time when the particle concentration reaches the maximum
$t_{max,i}$	Time when the concentration in size bin i reaches the maximum
α	Ion–ion recombination coefficient
Δt	Time difference
χ	Ion–aerosol attachment coefficient

direct observation of clusters and freshly formed particles (<3 nm) is now possible. Here, we present a step-by-step procedure to calculate J_{dp} values and GRs from chamber experiment data. Following equipment setup and calibration, the procedure starts by determining particle GR, followed by calculating different loss corrections (dilution loss, wall loss and coagulation loss) needed for obtaining the final particle J_{dp}. The last step is to estimate the error on J_{dp} values and GRs. We present the required instruments and their operation for obtaining accurate data, explain the procedures for calculating J_{dp} and GR, and troubleshoot errors that might occur during chamber experiments or analysis.

Alternative methods

Generally, the main parameter describing the NPF intensity is the formation rate, J_{dp}, that is, the rate at which particles are formed per unit volume per unit time at a given particle diameter d_p (ref. [7]). Preferably, d_p is in the range of 1.5–2 nm, which is close to the size of the critical cluster, that is, the smallest stable particle. In this case, the formation rate can be called the nucleation rate. In many previous laboratory studies, the ability of a given system to produce new particles was characterized by the rate at which new particles appeared, dN/dt, termed the apparent formation rate (J_{ap}). As such, this method may be internally consistent in a single experiment, but the comparability of the results to different reactors or field data is limited, owing to different loss processes affecting the measured concentration. No unified method has been introduced in the literature to correct dN/dt for particle losses due to dilution and scavenging onto existing particle surfaces or reactor walls to obtain J_{dp} for chamber measurements. In addition, to obtain the nucleation rate, J_{dp} has often been measured at the size of 3 nm, or even larger, and then theoretically extrapolated to 1.5 nm[115,116]. Although theoretically sound, this method relies on several assumptions, such as a constant particle GR[117] and negligible self-coagulation[118]. Other parameters that have been used for describing the NPF intensity in chamber or flow tubes include total number concentration of particles generated and apparent formation rate[57,110].

The variety of parameters and methods to quantify NPF makes it difficult to compare obtained results, because different methods can yield different results, even for the same dataset. Kulmala et al.[114] presented a standard procedure to analyze J_{dp} values and GRs from atmospheric data. However, to our knowledge, a similar protocol for chamber observations has been lacking until now.

Advantages and limitations

The main advantages of this protocol compared to previous approaches are that J_{dp} values and GRs are measured and analyzed directly at the size of the forming clusters and that the protocol is specific to chamber experiments.

The main limitation of this protocol is that, although the same basic principles apply for all experiments, the precise calculations need to be modified depending on the specific characteristics of the chamber in question and the instrumentation used. In addition, experimental data from chambers might not always be directly comparable to atmospheric observations because of the different aerosol and chemical reaction dynamics, missing vapor and aerosol constituents, or poor representation of atmospheric processes such as oxidation.

Applications

The methods for analyzing NPF from atmospheric and chamber data differ because of differences in the dynamics and the spatial and temporal scales of NPF in the chamber as compared with the atmosphere[118]. In the atmosphere, particle formation often occurs over a large geographical area and particle concentrations can change because of processes other than nucleation, such as primary particle emissions and horizontal or vertical transport of particles[119–122]. In addition, the particle sinks are different. The main sink for newly formed particles in the atmosphere is coagulation onto the existing particle population[123], whereas in chamber experiments, particle losses to chamber walls are normally much more important than coagulation[118] because the existing particle population is usually absent or small. Furthermore, in the atmosphere, the intensity of particle formation changes during the course of the day because the concentrations and properties of precursor vapors are constantly changing depending on environmental conditions such as solar radiation intensity. In a chamber, the production rate of precursor vapors can usually be kept constant for hours, and several variables characterizing NPF can be averaged over this period.

Experimental design

To quantify the particle dynamics during a controlled NPF chamber experiment, a set of instruments is needed to measure the size distribution of the particles from the initial cluster formation size (~1 nm) to the maximum size they reach during the particle growth process. Whereas measurements of particle number concentration and size distribution at small sizes (preferably <3 nm) are needed for calculating the J_{dp} value and initial GR, a measurement of the size distribution extending to larger sizes is required for the determination of coagulation sink and growth to larger sizes (Table 2). To quantify the gas phase concentrations of the vapors participating in NPF and their precursors, as

Table 2 | Recommendations for the measurement of relevant trace gas concentrations

Quantity to be measured	Importance
Total particle number concentration above ~1.5 nm	Required for determining J_{dp}
Particle size distribution covering the size range of ~1–1,000 nm (upper diameter depends on the experimental plan)	Required for determining the particle GRs, and coagulation and condensation sinks
Ion size distribution	Required for studying of role of ions in particle dynamics
Trace gas concentrations	Required to quantify the precursor concentrations and to monitor chamber cleanliness
Concentration and composition of vapors and clusters directly participating in NPF	Required to understand the mechanism and intensity of the NPF process
Accurate measurement of temperature and RH	Required for determining the exact characteristics of the experiment

well as to ensure the cleanliness of the chamber, a measurement of relevant trace gas concentrations is required (Table 2).

Requirements for particle measurements

Two categories of particles should be measured: (i) particles that result from the NPF and growth process (e.g., precursors, oxidation products) and (ii) background particles that should be monitored to ensure the cleanliness of the chamber (to ensure that NPF is a consequence of the precursors and the processes associated with them).

The concentration measurement accuracy and cutoff diameter of the condensation particle counters (CPCs) should be verified. ±10% accuracy or better is recommended for the concentration measurement, and users should adhere to a ±0.2-nm accuracy for the CPC cutoff diameter to ensure an accurate derivation of growth and nucleation rates. To minimize errors, we recommend that the cutoff diameter of the CPC be the same as the diameter at which the J_{dp} value is determined. The verification should be done by using a particle composition and concentration similar to those produced in the chamber experiments. See 'Instrument calibration' in the 'Equipment setup' section in the Materials for further discussion of accurate measurements of sub-3-nm particles.

Multiple size distribution measurement instruments are required to cover the whole size range of 1–1,000 nm (upper size diameter depends on experimental design). An overlap in the size range between instruments is important to ensure comparability. Laboratory calibrations, side-by-side comparisons and combined size distributions are essential to obtaining an agreement between the instruments at overlapping size ranges. Multi-instrument inversion routines are beneficial, if available.

Time resolution should be as high as possible, especially during periods of rapid particle formation and growth. For instance, in the case that the GR in the chamber is 60 nm hr^{-1}, an instrument with 1-min time resolution is needed to capture the concentration at each d_p. The time resolution should be optimized considering the particle concentration, instrument sensitivity and statistics[124]. Table 3 summarizes the commercially available particle number concentration instruments and their respective time resolutions.

Total particle concentrations can vary from very low (<10 cm^{-3}) to very high (>10^6 cm^{-3}). For an accurate determination of J_{dp} and GR, the instruments need to measure the total particle concentrations and size distributions accurately over a wide concentration range. At low concentrations (<1,000 cm^{-3}), the performances of both particle size magnifiers (PSMs) and condensation particle counter batteries (CPCbs) for particles <5 nm are better than those of electric mobility spectrometers (EMSs), which suffer from high particle losses and low charging probabilities. On the other hand, at high concentrations (>10^6 cm^{-3}), the performance of EMSs is usually not affected, whereas the accuracy of CPCs in measuring total particle concentrations is affected by a coincidence in the optics[125,126]. Depending on the CPC type, a coincidence correction can be applied for concentrations up to ~10^5–10^6 cm^{-3}; above that, the CPC signal typically becomes saturated.

Particle losses, especially in the sub-10-nm size range, are high. This should be considered when designing the sampling lines and selecting instruments. See 'Equipment setup' in the Materials section for further discussion of particle loss prevention measures and corrections.

Table 3 | Instruments for measuring sub-3-nm particle formation and growth

Abbv.	Instrument	Size range	Type of particle measurement	Time resolution	Details	Reference
PSM	Particle size magnifier	>1 nm/1–3 nm	Total concentration/ size distribution	1 s/2 min (scanning)	DEG & butanol/ water	Vanhanen et al.[173]
DEG CPC[a]	Diethylene glycol-condensation particle counter	>1 nm	Total concentration	1 s	DEG & butanol/ water	Wimmer et al.[176], Jiang et al.[180]
CPC[a]	Condensation particle counter	Typically >2.5 nm or >7 nm, depending on model	Total concentration	1 s	Butanol or water	Stolzenburg and McMurry[174], Hering et al.[201]
CPCb	Condensation particle counter battery	1–10 nm, depending on CPCs	Total concentration/ size distribution	1 s	DEG, butanol and/or water	Kulmala et al.[185]
DMA train	Differential mobility analyzer-train	1.6–8 nm	Size distribution	10 s	DEG and butanol and/or water	Stolzenburg et al.[179]
SMPS[a]	Scanning mobility particle sizer	1.5–1,000 nm (smaller for each instrument type/model)	Size distribution	~1–5 min, depending on model and size range	DEG, butanol or water	Wang and Flagan[177]
NAIS	Neutral and air ion spectrometer	2.5–42 nm (total), 0.8–42 nm (charged)	Size distribution, ion size distribution	10 s	NA	Mirme and Mirme[178]
CIC	Cluster ion counter	<3 nm	Ion size distribution	10 s	NA	
AIS	Air ion spectrometer	0.8–42 nm	Ion size distribution	10 s	NA	Mirme et al.[202]

NA, not applicable. [a]Many different commercially available or in-house-built models/sub-types exist.

Requirements for measurements of gaseous species

Two categories of gaseous species should be measured: (i) compounds that participate in the NPF and growth process (e.g., precursors, oxidation products) and (ii) compounds that are monitored to ensure the cleanliness of the chamber (to ensure that NPF is a consequence of the precursors and the processes associated with them).

The concentrations of relevant trace gases that may be introduced into the chamber, such as SO_2, NO_x and O_3, must be measured. SO_2 usually serves as a precursor for H_2SO_4, NO_x affects the formation of oxidized organic vapors, and O_3 is the main oxidant of many unsaturated organic species and is also used to produce OH radicals through photolysis (with UV light of ~248-nm wavelength) or by reacting with alkenes (e.g., tetramethylethylene). In most chamber experiments, concentrations of these trace gases are well above 1 p.p.b. and can be accurately measured by trace-gas monitors, which typically have a detection limit of ~0.5 p.p.b. In experiments that aim to simulate pristine environments, very low concentrations of SO_2 and NO_x are required and more advanced instruments are needed. Cavity-attenuated phase shift (CAPS)[127] can be used to measure NO_2 with a detection limit of 0.1 p.p.b. (3-σ, 10-s time interval). The CLD 780 TR (chemiluminescence detector)[128] is able to measure NO with the lowest detection limit of 3 p.p.t. SO_2 can be also measured with a chemical ionization mass spectrometer (CIMS) using CO_3^- as the primary ion[98], which has a detection limit of 15 p.p.t.

Volatile organic compounds (VOCs) should be measured, and the most commonly used instrument for this purpose is a proton-transfer-reaction time-of-flight mass spectrometer (PTR-TOF)[129–131]. The detection limit of the PTR-TOF is a few p.p.t., much lower than the required VOC concentration in most chamber studies. Some VOCs oxidize to form HOMs (highly oxygenated molecules) and other low-volatility organic vapors, which are important precursors for NPF, whereas some are present in the chamber as contaminants and might not influence NPF.

H_2SO_4, which is generally regarded as the most important NPF precursor in the atmosphere, can be measured by a chemical ionization atmospheric-pressure-interface time-of-flight mass spectrometer (CI-APi-TOF) using NO_3^- as the primary ion[132]. Calibrations need to be performed before and after the experiments[133]. HOMs can also be measured with the nitrate-ion-based CI-APi-TOF[23]. Because many different HOMs have very similar masses, the mass resolution of the instrument is critical. The detection limit of the CI-APi-TOF is ~1 p.p.q. We suggest a minimum mass resolution of 4,000 mass divided by mass difference ($m/\Delta m$), but a higher mass resolution is always preferable.

Table 4 | Chambers used for studying sub-3-nm particle formation and growth

Chamber Name	Unit material	Volume	Particle measurement instrument (cutoff)	Calculated quantities used in NPF analysis	References
Cosmic Leaving Outdoor Droplets (CLOUD)	Stainless steel	26 m^3	PSM (<2 nm), CPC (~3 nm), NAIS, SMPS	$J_{1.7}$, GR	Kirkby et al.[54], Almeida et al.[74], Riccobono et al.[77], Tröstl et al. [85], Kirkby et al.[98], Duplissy et al.[96], Lehtipalo et al.[102], Kürten et al.[203]
Forschungszentrum Jülich Plant Atmosphere Chamber (JPAC)	Borosilicate glass	1.45 m^3	PSM, CPC (TSI 3025A, 3 nm), SMPS (15–600 nm)	J_1	Dal Maso et al.[86]
Experimental Multiphasic Atmospheric Simulation Chamber (CESAM)	Teflon	4.2 m^3	NAIS	$J_{3,ap}$	Boulon et al.[87], Wang et al.[88]
National Center for Atmospheric Research (NCAR)	Teflon	10 m^3	DMA-TRAIN	GR	Pichelstorfer et al.[89]
Paul Scherrer Institute	Teflon	27 m^3	CPC battery, SMPS	$J_{1.5}$[a]	Paulsen et al.[93], Metzger et al.[94], Riccobono et al.[95]

[a]$J_{1.5}$ was scaled back from J_3.

Although it remains a challenge to perform direct calibrations for HOMs, it is reasonable to assume that the detection efficiency of HOMs is the same as that of H_2SO_4[23]. In addition, because the mass-to-charge ratio (m/z) of HOMs varies widely over the mass spectrum, the mass-dependent transmission bias of the mass spectrometer needs to be corrected[134].

Low-volatility or semi-volatile organic compounds, which probably do not directly nucleate but are likely to contribute to subsequent particle growth, should preferably also be monitored. These compounds can be measured with a high-resolution time-of-flight chemical ionization mass spectrometer (HR-tof CIMS) using, for example, iodide[135] or acetate[136] as reagent ions, or with a recently developed PTR[137,138]. As with HOM measurements, we suggest a minimum mass resolution of 4,000 $m/\Delta m$ be applied when using these instruments.

NH_3 and amines can be measured with an HR-tof CIMS using ethanol[139], hydronium[140], or nitrate[141] as reagent ions. Because these vapors are tend to stick to surfaces, a heated sample inlet is recommended. Masses of amine compounds are usually close to the masses of amide compounds, and a mass resolution of 4,000 $m/\Delta m$ is needed to separate them. Besides CIMS, ion chromatography is also a technique that can possibly be used to measure NH_3 and dimethylamine[142]. Both measurement techniques show a detection limit of a few p.p.t.v. for NH_3 and amines.

The chemical composition of charged embryonic clusters can be measured with an atmospheric-pressure-interface time-of-flight mass spectrometer[143] (APi-TOF). This instrument is similar to the CI-APi-TOF, but does not use active chemical ionization (i.e., it measures naturally charged ion clusters). With a properly calibrated and tuned transmission efficiency, this instrument can measure the composition of charged clusters up to 3,000 Thomsons. This instrument can be operated in either a positive or negative mode. In the positive mode, NH_4^+ is the most typical charge carrier[144], whereas in negative mode, NO_3^- and HSO_4^- are the main charge carriers[145,146].

In addition to the two main types of gases that are involved in the chemical reactions and NPF mechanism inside the chamber, a dilution tracer can be used to estimate the dilution lifetime of reactants and products within the chamber. The gases used for this purpose, such as argon or CO_2[147–155] (although SF_6 was used in several early experiments, it has been subject to a worldwide ban since January 2006), should not be a byproduct of the reaction and should not stick to the wall. The dilution tracer is needed only when the chamber in use is not well mixed. If the chamber is well mixed and both total volume and flow are known, the dilution lifetime can be calculated using the inverse of Eq. 4.

Chamber considerations and requirements

Chamber characteristics vary widely, depending on the specific applications and building specifications (Table 4). The main varying features are size, irradiance, wall material, and temperature and pressure control. Many of the currently available chambers are made of Teflon, Pyrex, quartz, aluminum or stainless steel[46,88]. Although Teflon chambers are expandable and non-sticky, they are not electrically conductive, causing efficient ion scavenging and preventing studies of atmospheric nucleation mechanisms, in which the particle charge might play a crucial role. Teflon has been found to be a sink for organic vapors and particles[48,147,156]. Yet this material can be used outdoors under 'real' natural radiation conditions or indoors under more controlled temperatures for studying particle growth and chemical mechanisms related to particle formation. Compared with Teflon chambers, stainless-steel reactors are more robust (i.e., leakproof) at various pressures and electrically conductive, so they are more suitable for studying ion processes. Similarly, glass chambers are robust and can be easily cleaned and operated at low-pressure conditions. However, the irradiance in such chambers cannot be controlled. Glass and Pyrex are typical materials for flow tubes[110]. Chamber walls are required to be as smooth as possible because rough surfaces have been found to enhance particle deposition[109].

None of the reactor types are flawless; each suffers from unwanted features that may vary depending on the chamber size and material. For instance, common problems for all chambers are the wall losses of particles and gaseous species, inhomogeneity, difficulty in attaining vapor and particle concentrations similar to the atmosphere, and possible contamination issues. Most of these problems can be largely avoided by using large-volume chambers with a small surface-to-volume ratio. Thorough characterizations of chamber reactors have already been presented in the literature[20,46,88,110,151,157–159], but the critical characteristics of chambers for studying atmospheric NPF are as follows:

- *Minimal contamination*. Materials of the chamber walls and sampling ports must be cleanable (e.g., by water, heating and/or ozone treatment) in order to remove all chemical compounds that may affect the particle formation process. Note that certain compounds, such as ammonia, stick to surfaces and may be re-released when thermodynamic conditions change. See 'Chamber setup and cleaning' in the 'Equipment setup' section of the Materials section for a discussion of and recommendations for chamber cleanliness. In addition, the gas injection system (including mass flow controllers, valves and so on) must not introduce any additional contaminants. The concentration levels of potential particle precursor vapors (e.g., ammonia, amines, sulfuric acid, organics, iodic acid) need to be monitored with instruments that have low enough detection limits (parts per trillion volume level) to detect possible contaminants.
- *Homogeneous mixing*. There should be no gradients or hotspots of precursor concentrations or vapor supersaturations in the chamber. Characterization of homogeneity can be done via sampling from multiple ports complemented with flow simulations. A suitable configuration of fans (location, fan speeds) is needed to mix the air, depending on the chamber geometry. There should be a balance between mixing and particles losses. If a laminar flow is not available, a counterflow fan should be used for mixing[20,46,88,160,161].
- *Equal charge distribution*. All materials should be electrically conductive to avoid ion losses. In addition, a high-voltage clearing field can be used to filter away ions to study purely neutral processes.
- *Large chamber volume*. The chamber volume needs to be large, so that the particle residence time is long enough, because the chamber air is constantly diluted to compensate for the air consumed by the measurement instruments. Typical time scales of the particle formation and growth processes are from minutes to hours when using atmospheric concentration levels. Although a spherical configuration would have the highest volume-to-surface ratio (i.e., maximum volume for minimum surface), such a configuration is very difficult to operate, clean and illuminate and is also associated with inefficient mixing[162]. A cylindrical configuration is recommended instead. The choice of a chamber volume depends on the aim of the experiment, especially the required maximum size of the particles, as well as on precursor concentrations and thus the dilution lifetime.
- *Chamber flow rate*. The total volumetric flow rate required by all the sampling instruments should be considered when designing the chamber flow system and volume. Efficient sampling of sub-5-nm particles requires high sample transport flows to the instruments (see 'Equipment setup' in the Materials section), which increases the required total flow rate from the chamber. To maintain chamber purity, no backflows from the instruments should be allowed, so there should always be a small overpressure inside the chamber. Particle and vapor measurement instruments should be placed as close to the chamber as possible in order to minimize losses in inlet lines.
- *Chamber stability*. The chamber temperature, irradiance (and other external conditions), and gas flow rates must remain stable, so that experiments are reproducible. Particle formation rates (J_{dp} values) should not vary by >5% for at least 12 min (three consecutive full PSM scans, depending on instrument time resolution).

Flow tube design

The design of flow tubes can vary, but they usually consist of four sections: an inlet system, a mixing unit, a nucleation unit and an outlet where sampling takes place. The inlet system design depends on the precursor gas. In H_2SO_4 nucleation experiments, H_2SO_4 can be point-produced from a liquid solution and then injected into the flow tube or it can be generated in situ from SO_2 gas. The point-production from liquid solution is achieved either by atomizing a liquid solution followed by vaporization using a furnace[51,65,67,69] or by flowing carrier gas over a temperature-controlled reservoir[52,58,68,73,78,111]. Alternatively, in situ generation of H_2SO_4 involves production of OH radicals from photo-dissociation of H_2O vapor[61,63,71,72,83] or ozone photolysis by UV light[59,60,62,64,67]. The injection of other gases is usually achieved by using the same techniques, by applying several dilutions from concentrated gas bottles or by using permeation tubes.

In the mixing unit, the precursor gas (or gas mixture) is mixed with the carrier flow. The method by which the gas flow is introduced, together with the profile of the mixing, determines the distance needed for laminar flow to develop downstream of the mixing unit. For this purpose, simple plug-type inlets, perforated Teflon manifolds, showerhead inlets, spoke inlets, diffusers and transition cones are commonly used.

After mixing, nucleation should take place in the nucleation unit, which is kept at an approximately constant temperature using cooling jackets. The nucleation unit is typically made of glass, although stainless-steel and Teflon-lined stainless-steel units can also be used (Table 5). In studies in which photolysis is needed, the nucleation unit can be irradiated with UV light[59,60,62,64]; otherwise, gases such as ozone can be irradiated before entering the nucleation unit[61,63,71,72,83].

Finally, particle-measuring instruments are connected to the outlet of the flow tube. The choice of the particle-measuring instrument can have substantial effects on the measured particle number concentration and therefore on calculated J_{dp} values. In nucleation experiments, we are interested in measuring sub-3-nm particles, so the instrument must be chosen accordingly. Nevertheless, the measured particle number concentration at the end of the flow tube also depends on the nucleation and growth processes taking place across the length of the flow tube. For these reasons, the measured formation rate at the end of the flow tube might not be equal to the actual formation rate, so we refer to the 'apparent formation rate' (J_{ap}) when using flow tubes.

The calculation of formation rates in flow tubes $\left(J_{ap} = \frac{N}{\Delta t}\right)$ is similar to that for formation rates in chambers, yet it does not include the particle loss mechanisms (wall loss and coagulation loss), which are usually considered to be negligible in short reaction times. In the calculation, N is the number concentration of particles measured at the outlet of the flow tube and Δt is the characteristic time frame during which nucleation occurs[110]. If nucleation is homogeneous across the nucleation unit of the flow tube, then Δt is equal to the residence time. Consequently, Δt is simply calculated from the flow rate and volume of the nucleation unit. If nucleation is not homogeneous across the nucleation unit, a proper characterization (through experiments or flow simulations) of the flow tube must be performed to determine the real nucleation zone and the real nucleation time (Δt). Under these circumstances, Δt can range from 10% to 60% of the residence time[51,52,63,65,72].

Multiple factors can affect the nucleation homogeneity inside the nucleation unit, for example:

- Buoyancy and thermally driven convection are likely to take place at the entrance of the nucleation unit, and the flow regime might not be fully laminar.
- Possible temperature gradients between the mixing unit and the nucleation unit might induce undesirable particle production at the entrance of the nucleation unit.
- Across the flow tube, the gas mixture composition is likely to change because precursor gases have reacted away or have been lost to the walls, rendering nucleation negligible beyond a certain point.
- Point production of gases from liquid samples is known to produce a non-uniform gas profile in the flow reactor as compared with in situ production[63,67,71].

Error estimates for the apparent nucleation rate must include errors associated with particle-counting instruments and inaccuracies in the determination of the nucleation time. Additional errors can be caused by neglecting wall losses and coagulation losses.

Wall losses in flow tubes have a more severe effect on precursor gases than on particles, so proper corrections must be applied to determine the exact precursor gas concentration at which nucleation takes place. Particle wall losses become important in the case of turbulent flows, high residence times or large surface-to-volume ratios of the flow tube (e.g., due to small inner diameters). Ideally, one can assume that the particle wall loss rate is of first order and determine it experimentally by introducing particles of a certain size into the flow tube and measuring their concentrations at different positions

Table 5 | Flow tubes used for studying sub-3-nm particle formation and growth

Institute/collaboration	Nucleation unit material	Unit dimensions; length (cm) × i.d. (cm)	Particle measurement instrument (cutoff)	Calculated quantities used in NPF analysis	Reference
Finnish Meteorological Institute	Stainless steel	200 × 6	UCPC TSI 3025A (2.18 nm)	J_{ap}	Brus et al.[65]
			UCPC TSI 3025A (2.8 nm) & PSM	J_{ap}	Brus et al.[69]
			PHA-UCPC (<2 nm) & PSM	J_{ap}	Sipilä et al.[67]
	Stainless steel with inner Teflon coating	255 × 10.95	CNC TSI 3020	J_{ap}	Viisanen et al.[51]
Kent State University	Pyrex	82 × 5.08 or 80 × 2.54	SMPS TSI 3936N76/UCPC TSI 3786	J_{ap}	Benson et al.[61] Young et al.[63]
		85 × 12.8	UCPC TSI 3786 (2.3 nm)	J_{ap}	Benson et al.[71], Yu et al.[72]
Nanjing University of Information Science and Technology	Teflon	90 × 5.08	CPC TSI 3776 & PSM	$J_{1.7}$[a]	Yu et al.[83]
Leibniz Institute for Tropospheric Research (TROPOS)	Teflon	449 × 8	UCPC TSI 3025 (3 nm)	J_{ap}	Berndt et al.[59], Berndt et al.[60], Berndt et al.[62]
			UCPC TSI 3025 (3 nm), PHA-UCPC (1.5 nm) & PSM	J_{ap}	Berndt et al.[64], Sipilä et al.[67]
Texas A&M University	Pyrex	60 × 2.45	UCPC TSI 3025A (3 nm)	$N_{>3}$	Zhang et al.[58], Wang et al.[68]
University of Alabama in Huntsville (TANGENT – FT1)	Pyrex	80 × 4.85	PSM TSI SMPS (3080) & CPC (3776) (>3 nm)	J_0[b]	Benson et al.[61], Young et al.[63], Benson et al.[71], Tiszenkel et al.[204], Benson et al.[205], Erupe et al.[206]
University of Delaware (TANGENT – FT2)	Quartz	152 × 20	SMPS (TSI 3938, 3788)	$GR_{>2}$	Tiszenkel et al.[204], Krasnomowitz et al.[207], Stangl et al.[208]
Augsburg College University of Minnesota	Glass	105 × 5	UFCNC UCPC	J_{ap}	Ball et al.[52] Zollner et al.[73], Glasoe et al.[78] Jen et al.[76], Jen et al.[81]
University of California Irvine	Borosilicate glass	110 × 7.6	TSI SMPS (2.5 nm)[c]	$N_{>2.5}$	Chen et al.[79], Chen et al.[80]
			TSI SMPS (2.5 nm) & PSM	J_{ap}	Chen and Finlayson-Pitts[84]
Caltech	FEP Teflon	2 × 28	CPC (TSI 3025: 3 nm; TSI 3010: 6 nm), SEMS (25–700 nm)	$N_{>3}$	Jimenez et al.[57]

[a] $J_{1.7}$ is calculated from particle number concentration and decay of sulfuric acid. [b] J_0 represents the nucleation rate corresponding to the initial sulfuric acid concentration; see Tiszenkel et al.[196]. [c] Detection efficiency estimated to be <1% for 3-nm particles due to sampling losses.

Box 1 | Recommendations for flow tube experiments

- Residence time inside the flow tube must be high enough to allow for particle growth to diameters larger than the cutoff of the particle-measurement instruments, yet low enough that wall losses will not become important.
- Increasing the inner diameter of the flow tube helps reduce wall losses.
- Experiments should be started with the lowest concentrations and highest RH, and ended with the highest concentrations and lowest RH.
- We recommend keeping a continuous flow of nitrogen through the flow reactor when it is not used in experiments to minimize the exposure of the reactor to room air.
- In the case of point production of H_2SO_4, care must be taken to minimize H_2SO_4 decomposition to SO_3 in the liquid reservoir or downstream of it.
- In the case of point production of H_2SO_4, Teflon filters or glass frits should be used in order to remove any liquid residue or particulate impurities.

inside the tube[163]. Introducing a laminar sheath flow to prevent the sample flow from contacting the wall may be an option to reduce wall losses[164], yet a precise control is needed in such complex designs.

Coagulation losses become important and cannot be neglected if (i) all particles form immediately ($\sim t_0$) and the residence time inside the flow tube is sufficient for particles to interact, (ii) the time scale of the coagulation process is comparable to that of the nucleation process, or (iii) the particle concentration is high. An upper limit of coagulation can be determined from the measured particle size distribution and by estimating coagulation rate constants as a function of particle size. Additional recommendations for operating flow tubes are presented in Box 1.

Method for determining particle GR

The particle GR is defined as the rate of change of the diameter, d_p, representing the growing particle population (see also Kulmala et al.[114]):

$$\mathrm{GR} = \frac{dd_\mathrm{p}}{dt} \quad (1)$$

Particle GRs can be determined by following the time evolution of the particle number size distribution during a particle formation event. This can be done by using different methods, including the log-normal distribution function method (which is not covered in this protocol because it is often unsuitable for chamber experiments, being that there are no distinct particle modes)[114], the maximum concentration method (Step 2A; Lehtinen and Kulmala[165]), the appearance time method (Step 2B; Lehtipalo et al.[166]), and different general dynamics equation (GDE)-based methods (Step 2C; Pichelstorfer et al.[89], Kuang et al.[167]).

For GDE-based methods, the time evolution of the aerosol number distribution $n(d_p,t)$ is described by the so-called GDE, which in its continuous form can be written as

$$\frac{\partial n(d_\mathrm{p},t)}{\partial t} = \frac{1}{2}\int_0^{d_\mathrm{p}} K\left(\sqrt[3]{d_\mathrm{p}^3 - d'^3_\mathrm{p}}, d'_\mathrm{p}\right) n\left(\sqrt[3]{d_\mathrm{p}^3 - d'^3_\mathrm{p}}, t\right) n(d'_\mathrm{p}, t)\, dd'_\mathrm{p} - n(d_\mathrm{p}, t)\int_0^\infty K(d_\mathrm{p}, d'_\mathrm{p})\, n(d'_\mathrm{p}, t)\, dd'_\mathrm{p} - \frac{\partial}{\partial d_\mathrm{p}}\left(\mathrm{GR}(d_\mathrm{p})\, n(d_\mathrm{p}, t)\right) + Q(d_\mathrm{p}, t) - S(d_\mathrm{p}, t) \quad (2)$$

Here $K\left(d_p, d'_p\right)$ is the coagulation coefficient between particles of diameters d_p and d'_p, and $Q(d_p,t)$ and $S(d_p,t)$ are the source and sink terms, respectively, for particles with diameter d_p. In a typical chamber experiment, the only source of particles is nucleation and the sink term arises from wall deposition.

In our typical problem setup, the time evolution of the number distribution function $n(d_p,t)$ is measured and the coagulation coefficients $K\left(d_p, d'_p\right)$ are sufficiently well predicted by theory. Lehtinen et al.[168] applied simple least squares based optimization to solve the unknown $\mathrm{GR}(d_p)$ and $Q(d_p,t)$ for atmospheric field data measured in Hyytiälä, Finland, assuming size-independent growth and neglecting deposition. This method was later improved (with more processes and fewer assumptions) by Verheggen et al.[169] and Kuang et al.[167]. None of these methods, however, is suitable for rigorous estimation of errors in GR (or Q).

Different GR methods have been compared using measurement and simulation data[89,170–172], and they have been found to agree reasonably well in most conditions. GR methods can be applied to data measured with different particle-sizing instruments, which enables determination of GR for different size ranges or comparison of GR values for same-size particles from different instruments. GRs can usually be determined more accurately from chamber experiments than from atmospheric measurements because there is less fluctuation in the data, as well as more accurate particle size distribution measurements. Estimation of uncertainties in GRs is explained in Steps 8 and 9.

Materials

Reagents

For operation of instruments (depending on setup)

- 1-Butanol, reagent grade (VWR 20808.325) **! CAUTION** Butanol is flammable and corrosive. It causes skin irritation and serious eye damage and may cause respiratory irritation. While using butanol, wear protective gloves and eye protection, and work in a well-ventilated area. Keep it away from heat and ignition sources.
- Diethylene glycol, reagent grade (DEG; VWR 8.03131.5000) **! CAUTION** Diethylene glycol is harmful if swallowed and may be combustible at high temperatures. Wear protective gloves and eye protection while handling.
- Nitric acid (Fisher Chemical N/2300/PB17) **! CAUTION** Nitric acid is flammable, highly corrosive and toxic. It causes severe skin burns and eye damage. Wear protective gloves, protective clothing, eye protection, and face protection while using nitric acid. Use it only in a well-ventilated area away from heat, hot surfaces, sparks, open flames and other ignition sources.

For conducting the experiment

- Synthetic air (or atmospherically relevant mixture of O_2 and N_2)
- Water (Milli-Q ultrapure[66])
- Ozone
- Suitable precursor gases, depending on which chemical system will be studied (e.g., SO_2, H_2SO_4, NO, NH_3, amines, volatile organic compounds, iodine)

Equipment

▲ CRITICAL A comparison of instrument types is shown in Table 3.

- Condensation particle counters (CPCs) together with a particle size magnifier (PSM), commonly known as a condensation nuclei counter[173–176]. A particle counter with a cutoff size ~1.5 nm is required for a total particle concentration measurement. It is preferable to have multiple CPCs at different cutoff sizes or a PSM operated in a scanning mode to measure size distributions between ~1 and 3 nm
- Electric mobility spectrometers (EMSs). Multiple EMSs are required for measuring particle and ion size distributions between ~1 and 1,000 nm. These include some varieties of scanning mobility particle sizer (SMPS)/differential mobility particle sizer (DMPS), neutral cluster and air ion spectrometer (NAIS), air ion spectrometer (AIS), cluster ion counter (CIC) and differential mobility analyzer-train (DMA-train)[177–180]
- Mass spectrometers (MSs). Multiple mass spectrometers are required for quantifying the precursors of NPF and for determining the composition of growing clusters. Suitable instruments include APi-TOF, CI-APiTOF and other chemical ionization MSs, and PTR-TOF instruments[132,137,143]
- Gas-measuring instruments. Trace gas monitors are required for measuring the relevant trace gases (e.g., O_3, NO, NO_2, SO_2, NH_3)
- Instrumentation to accurately monitor chamber conditions, such as temperature, pressure, relative humidity (RH), dew point, flow rates and (solar) radiation

Equipment setup

Chamber setup and cleaning

Cleanliness of the chamber is a key requirement for studying atmospheric NPF, as even a few p.p.t.v. of trace gases (e.g., ammonia) can have a tremendous effect on nucleation rates[54]. We recommend taking the following precautions:

- All gas supplies should be as clean as possible. One way to provide clean gases is to have them in liquid form. During evaporation, some of the contaminant gases will be trapped in the liquid.
- All pipelines going from the gas supply to the chamber should be made of stainless steel. Avoid connectors and mass flow controllers that contain plastic material and polytetrafluoroethylene (Teflon).
- A dedicated line for each trace gas is preferable to avoid memory effects from previous gases.
- Electropolishing of the chamber's inner surfaces is recommended to enable better cleaning (in stainless-steel chambers).

Box 2 | Recommendations for ensuring accuracy of the total concentration measurement

There are several ways to ensure the accuracy of the total concentration measurement, which is critical in accurately determining J_{dp}. These are as follows:

1. Calibrate the CPC cutoff size using particles of the same composition and a concentration similar to that of the chamber.
2. Compare total particle concentration measurements to integrated particle concentrations from size distribution measurements.
3. Measure the total concentration at multiple cutoff sizes (using scanning PSM or CPCb) and size distributions using an EMS (e.g., NAIS or nanoSMPS, which are usually composition independent) and compare their development over time (appearance times); see Fig. 1.
4. Use only straight laminar flow particle transport lines, and experimentally characterize the size-dependent particle penetration.
5. Correct the transport losses for the measured size-resolved particle size distribution.

- Clean water vapor can be made using a Permapore-type interface between the clean air carrier and clean recirculating liquid water, to ensure no contamination from the water supply. Note that a few parts per trillion of impurities in liquid water results in a few parts per quadrillion in the gas phase.
- Cleaning of the chamber walls before and between experiments can be done by using synthetic clean air of high humidity at high temperatures. High ozone concentrations can be used to remove contaminants from chamber wall surfaces with UV light on. The exact cleaning procedure depends on the chamber material and the chemical compounds used in the experiments.
- The chamber should be leakproof and have a slight overpressure to avoid any vapor and particle contamination from room air.
- Run a background or zero measurement before initiating any NPF process inside the chamber; measurement of precursor vapors and background particles should be done before precursor injection to ensure a contamination-free environment.

Instrument calibration

For accurate determination of J_{dp}, the concentration, sizing and cutoff diameter calibration of the instruments measuring the total particle concentration and size distribution are critical. The concentration response of particle counters should be verified against a reference instrument in the concentration range that is expected during the measurements. The cutoff diameter of a CPC must be verified, preferably with test particles that are similar to the particles produced during the chamber experiments, because the cutoff diameter is affected by the particle chemical composition and charging state[181–185]. The magnitude of the effect depends on the working liquid of the instrument, as well as on the particle composition.

During NPF, the size-resolved concentration of precursor vapors, molecular clusters and nanoparticles usually decreases rapidly with an increasing particle diameter. In the size range of 1–3 nm, this gradient is so high that a slightly erroneous CPC cutoff diameter causes a non-negligible error in the measured total particle concentration[186], which further accumulates into errors in J_{dp} calculations. Furthermore, changes in external conditions, such as pressure or sample temperature and RH, can affect the cutoff size and instrument performance in general[187]. Therefore, we recommend that the instrument be calibrated before the start of the experiment under the same environmental conditions as used for the experiment itself, using the same chemical composition of particles to be characterized (Box 2 and Fig. 1).

The sampling lines should be as short as possible. For straight lines with tubular and laminar flow, the particle losses can be estimated using the Gormley–Kennedy equation[188]. At the sampling line outlet, a core sampling system is needed to reduce the sampling losses and to maximize the signal at the particle counters[189]. Using transport flows to reduce the time for diffusional particle losses during transport from the chamber to the instrument may decrease particles losses in the sampling lines. The transport lines should be designed carefully to maximize the particle transport efficiency and signal in the detectors[190]. Any bends, elbows, valves, or splits cause distortion of the parabolic flow profile and will enhance particle losses as compared to laminar tubular flow. If these cannot be avoided, the particle penetration in the sampling line must be experimentally characterized to correct the size-resolved particle concentrations.

Evaporation of particles during sampling may be an issue, depending on the particle composition, especially when measuring very small clusters. Changes in the carrier gas temperature or composition (e.g., due to dilution, drying or bringing a cold sample to room temperature) should be avoided by using thermally insulated sampling lines and chamber air as carrier gas.

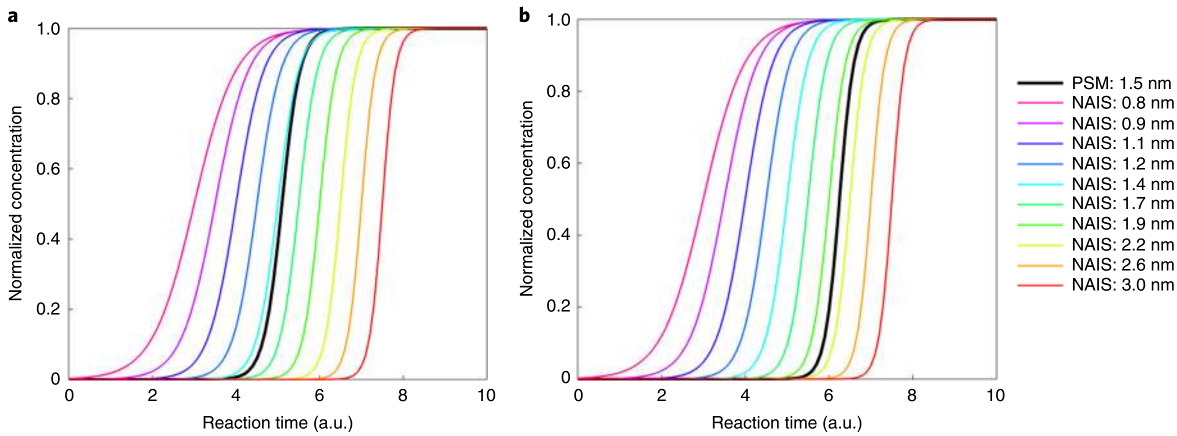

Fig. 1 | Simulated NPF experiment and instrument response. a,**b**, Comparison of the ion appearance times measured with the PSM at a nominal cutoff diameter of 1.5 nm (using the difference of total and neutral concentration from PSM measured without and with ion trap, respectively), and concentrations of ions measured with different size bins of the NAIS. The concentrations are normalized by the maximum concentration reached in the experiment (steady-state value). The PSM cutoff is determined correctly in **a**, whereas the cutoff is shifted (e.g., due to different particle composition compared to calibration) in **b**, and a correction is needed.

Procedure

Pre-injection measurement of chamber background

1 Start the NPF process by injecting the nucleating precursors and initiating their oxidation by injecting oxidant and/or illuminating the chamber with the required wavelength of radiation (Fig. 2).

▲**CRITICAL STEP** Measurement of precursors, particles and other parameters should precede the initiation of the NPF process to ensure chamber cleanliness (see 'Equipment setup' in the Materials section).

? TROUBLESHOOTING

Determining the GR

2 Particle GRs can be determined by either the maximum concentration method (option A), the appearance time method (option B) or the GDE method (option C). See the 'Experimental design' section for guidance on choosing one of these methods.

(A) **Maximum concentration method**

(i) Determine the times, $t_{max,i}$, when the concentration in each size bin i reaches the maximum. To obtain an accurate $t_{max,i}$ value, fit the concentration time series with a Gaussian function. An example of applying this method to chamber experiment data is shown in Fig. 3.

(ii) Plot the mean diameters of the size bins, $d_{p,mean,i}$, as a function of the maximum times, $t_{max,i}$.

(iii) Apply a linear fit to the size range at which the GR is determined.

(iv) Obtain GR as a slope of the linear fit (Fig. 3c). The maximum concentration method can also be used to estimate a size-dependent GR. It must be noted, however, that the ($t_{max,i}$, $d_{p,mean,i}$) pairs would then correspond to different times, which means that a 'pure' size dependence cannot be determined.

? TROUBLESHOOTING

(B) **Appearance time method**

(i) Determine the times, $t_{app50,i}$, when the concentration in each size bin i reaches 50% of the maximum concentration[86,166,171]. Unlike option A, this can be done by fitting a Sigmoid function to the concentration time series. Alternatively, one can determine the time, $t_{app,i}$, when the concentration in each size bin starts to rise. This can be done, for example, by determining the time when the concentration reaches 5% of the maximum concentration. It is also possible to determine $t_{app50,i}$ and $t_{app,i}$ from the total concentration measured with a CPC[95], instead of using the concentration in a certain size bin. Lehtipalo et al.[166] compared different methods to determine appearance times and concluded that the most robust method is to either determine $t_{app50,i}$ from size bin data or $t_{app,i}$ from total

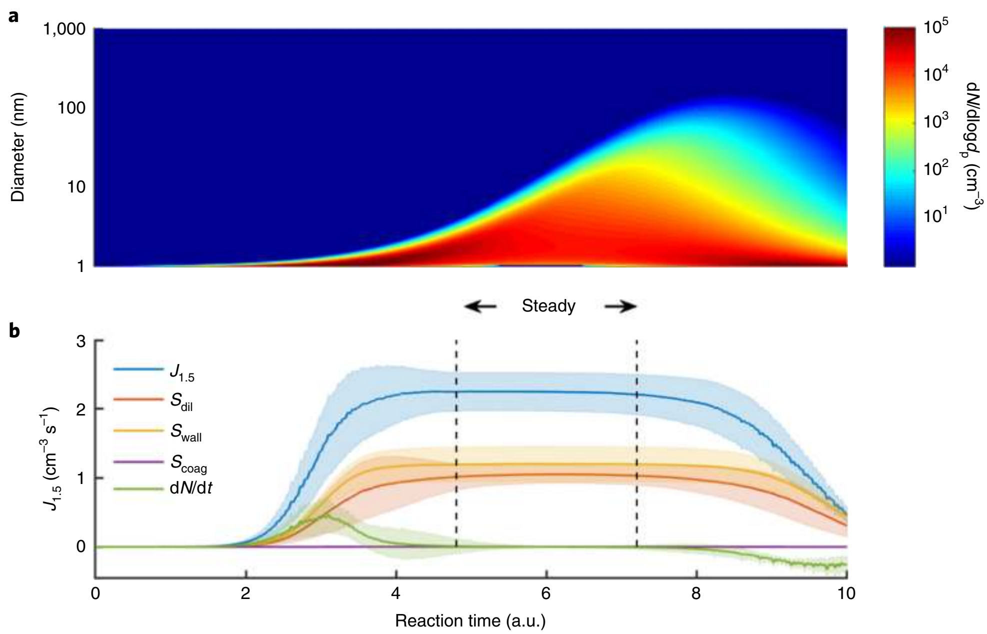

Fig. 2 | Anticipated results from an NPF experiment performed in a chamber. a, Simulated time evolution of particle size distribution during the experiment. **b**, Particle formation rate ($J_{1.5}$) and its different components. The shaded areas correspond to ±1σ uncertainty, obtained from the Monte Carlo simulation of 10,000 runs. The time between the dashed lines shows the time of the stable formation rate of particles (steady state), for which the average J_{dp} value should be calculated. The magnitude of the components and time scales varies depending on the chamber specifications, experimental plan (e.g., gas concentrations) and J_{dp} value and GR (affecting the particle size distribution).

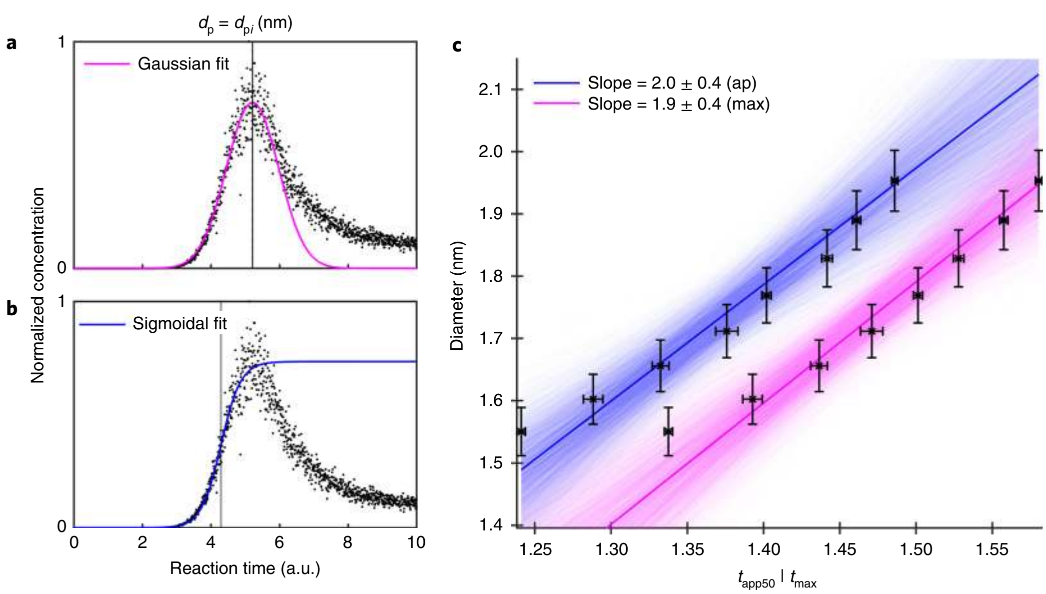

Fig. 3 | Calculation of GRs from chamber experiments using the maximum concentration method and the appearance time method. a, The concentration in a size bin is normalized by dividing it by the maximum concentration reached during the experiment and then fitting using a Gaussian fit. The same process is repeated for all the size bins for which a GR is calculated. **c**, The times corresponding to maximum concentration are then plotted as diameter versus time (t_{max}), as shown in magenta. The *x*-axis uncertainty is the ±1σ fit uncertainty from the Monte Carlo simulation of 10,000 runs, and the *y*-axis uncertainty is the estimated instrumental sizing uncertainty. GR is obtained as the slope of the linear fit to the d_p versus t_{max} data; GR = 1.9 ± 0.4 nm/h. The GR uncertainty is ±1σ from the Monte Carlo simulation. **b**, the concentration in a size bin is normalized by dividing it by the maximum concentration reached during the experiment and then fitted using a sigmoidal fit. The same is repeated for all the size bins for which a GR is calculated. **c**, The midpoints of the fits are then plotted as diameter versus time (t_{app50}), as shown in blue. GR is obtained as the slope of the linear fit to the d_p versus t_{app50} data; GR = 2.0 ± 0.4 nm/h. Note that the maximum concentration method gives the GR at a later time step during the experiment, so particle size distribution and gas concentrations in the chamber might have changed. app50, 50% appearance time; max, maximum.

concentration data. An example of $t_{app50,i}$ determined from the size bin data is shown in Fig. 3.

(ii) Plot the mean diameters of the size bins, $d_{p,mean,i}$, as a function of the appearance time $t_{app50,i}$ or $t_{app,i}$.

(iii) Apply a linear fit to the size range at which the GR is determined.

(iv) Obtain GR as a slope of the linear fit (Fig. 3). Note that the GR value might change with size, especially during the beginning of the growth process[85], in which case using a linear fit is a good assumption only in a narrow size range. It is also possible to fit a higher-order polynomial to the data points and obtain GR as a derivative of the curve.

? TROUBLESHOOTING

(C) **General dynamics equation method**

(i) Calculate the optimal match between the measured data and the solution to the GDE (see equation in the 'Experimental design' section). To solve the GDE, which is a partial-differential-integral equation, the continuous function $n(d_p,t)$ is typically approximated by a histogram, that is, by dividing the continuous-size spectrum into finite intervals (or bins), resulting in a set of ordinary differential equations for the bin concentrations $N(t)$. These ordinary differential equations can then be solved by standard numerical time integration routines.

(ii) Find the growth rate GR(d_p) and source rate $Q(d_p,t)$ corresponding to the optimal match. This can be done using different approaches. Our suggestion is to use the method by Pichelstorfer et al.[89], in which the GDE is fitted to the measured size distribution step by step. Starting from a measured size distribution at any time step, all the other aerosol dynamical processes are simulated first, on the basis of measured conditions and theory; then GR(d_p) is estimated by moving the distribution in size space in an optimal way to match the measured distribution at the next time step. In this way, by marching step by step in time, the dependence of GR is on both time and size can be estimated.

? TROUBLESHOOTING

Determination of particle losses

3 Determine dilution losses. If the chamber is operated in continuous mode, synthetic clean air should be continuously flowing into the chamber, and the instruments should be continuously sampling from the chamber. This leads to an artificially lower particle concentration in the chamber that is due to dilution, which needs to be corrected for when calculating J_{dp} values. The calculation for the loss rate of particles due to dilution is as follows:

$$S_{dil} = N_{>dp} \cdot k_{dil}[\mathrm{cm^{-3}\,s^{-1}}] \tag{3}$$

$$\text{with } k_{dil}[\mathrm{s^{-1}}] = \frac{\mathrm{Flow_{synthetic\,air}}}{V_{chamber}} \tag{4}$$

$N_{>dp}$ is the total particle concentration above the size at which you want to calculate the J_{dp} value, k_{dil} is the dilution rate, $\mathrm{Flow_{synthetic\ air}}$ is the flow rate of clean air, and $V_{chamber}$ is the volume of the chamber.

4 Determine wall losses. Diffusional losses of particles to the chamber walls (S_{wall}) can be determined empirically by observing the decay of the concentration of a specific compound having a known diameter (e.g., decay of sulfuric acid monomer concentration after its photochemical production has been stopped by turning off the UV lights). The obtained loss rate coefficient is inversely proportional to the mobility diameter in a size range <100 nm, where diffusional losses are the most critical[191], and can therefore be scaled and applied to correct for the losses of different-sized particles when calculating J_{dp} values. See also Schwantes et al.[110] and references therein. The calculation for the wall loss rate is as follows:

$$S_{wall}(T) = \sum\nolimits_i N_{dpi-dpi+1} \cdot k_{wall}\left(d_p, T\right)[\mathrm{cm^{-3}s^{-1}}] \tag{5}$$

$N(d_p)$ is the number concentration of particles with a mobility diameter d_p from the size distributions, and k_{wall} is an experimentally determined factor based on mixing, chamber conditions and dark decay of the reference species in the absence of particles.

In previous chamber experiments[97,102], the value of k_{wall} was determined from the theoretical temperature dependence of the diffusion coefficient, $D \sim (T/T_{ref})^{1.75}$ [192] and the wall loss dependence on the diffusion coefficient, $k_{wall} \sim (D)^{0.5}$; see also McMurry and Grosjean[108] and McMurry and Rader[159].

The calculation for this is as follows:

$$k_{wall}(d_p, T) = F \cdot \left(\frac{T}{T_{ref}}\right)^{0.875} \cdot \left(\frac{d_{p,ref}}{d_p}\right)[s^{-1}]. \quad (6)$$

Here, F is an experimentally determined factor based on mixing, chamber conditions and dark decay of the reference species in the absence of particles, $d_{p,ref}$ is the mobility diameter of the reference species, T_{ref} is the reference temperature at which the experimental loss rate was determined, and T is the studied chamber temperature. In this protocol, we recommend that this equation be used only when the mean diameter of the particle number size distribution is smaller than ~100 nm[159].

5 Determine coagulation sink (S_{coag}), which describes the loss rate of particles due to coagulation onto a pre-existing particle population. Calculate the coagulation sink for the particle size at which you want to calculate the J_{dp} value, using the measured particle number size distribution. The calculation for determining coagulation sink is as follows[193]:

$$S_{coag}(d_p) = \int k_{coag}\left(d_p, d'_p\right) n\left(d'_p\right) dd'_p \cong \sum_{d'_p=d_p}^{d'_p=max} k_{coag}\left(d_p, d'_p\right) N_{d'_p} [cm^{-3}s^{-1}] \quad (7)$$

$k_{coag}(d_p, d_p')$ is the Brownian coagulation coefficient for particles sizes d_p and d_p'. It is usually calculated by using the Fuchs interpolation between continuum and free-molecule regimes. For chamber experiments, the coagulation sink is often negligible at the start of the experiment, but increases as the particles grow and more particles are formed in the chamber (Fig. 2b).

Determining J_{dp} value

6 Determine the total particle formation rate, J_{dp}, defined as the net flux of new particles into the measurable size range, that is, across the lower detection limit (d_p) of the particle counter used. By integrating the GDE from the instrument detection limit up to infinity, we obtain the following balanced equation for calculating the total number concentration N:

$$\frac{dN}{dt} = J_{dp} - S_{dil} - S_{wall} - S_{coag} \quad (8)$$

By rearranging the terms in this equation, we can solve for J_{dp}[114], as shown in the equation below.

$$J_{dp} = \frac{dN}{dt} + S_{dil} + S_{wall} + S_{coag}[cm^{-3}s^{-1}] \quad (9)$$

dN/dt is the time derivative of the total particle concentration above a certain threshold (preferably close to 1.5 nm) and S_{dil}, S_{wall}, and S_{coag} are the loss rate of particles, described in Steps 3–5.

For chamber experiments, the formation rate can be calculated from changes in the total particle number concentration measured with a PSM or some other CPC, because nucleation is the only source of particles. The d_p value at which the formation rate is determined depends on the cutoff size of the instrument, which is assumed to be a step function. For atmospheric data, a certain size bin close to nucleation size is used instead of the total particle concentration[114] in order to eliminate the effect of other particle sources or particle transport.

? TROUBLESHOOTING

7 (Optional) Determine the ion nucleation rate using an ion trap in front of a particle-measuring instrument. The ion nucleation rate ($J^{\pm}$), which is the formation rate of naturally charged ions only, can be determined using two particle-measuring instruments (e.g., CPC or PSM) in parallel, one of which is equipped with an ion trap to remove all ions[97]. The total J_{dp} value is then calculated from the instrument without the ion trap (see Steps 3–6). The neutral fraction of the total particle formation rate ($J_{n,tot}$), which is different from the neutral formation rate (J_n) introduced later in Step 13, is calculated using the instrument with the ion trap (see Steps 1–6). Note that in this case the neutral particle formation rate includes the particles that are formed by recombination of ions

and are therefore detected as neutral particles ($J_{n,tot} = J_n + J_{rec}$). The ion formation rate (sum of both polarities) is the difference between J_{tot} and $J_{n,tot}$

$$J^{\pm} = J_{tot} - J_{n,tot} \tag{10}$$

Error estimation

8 Determine the error in the GR. When using the appearance time and maximum concentration methods, there are two sources of uncertainty: the fits used for determining the appearance times or maximum concentration times, and the particle diameter that is obtained from the instrument. If one of them is clearly greater than the other, apply weighted least square fit using the variable representing the smaller error as an explanatory variable (option A). If the two variables have errors of similar magnitude, a fitting method allowing for error in both variables (e.g., total least squares or geometric mean regression) should be used (option B).

(A) **Weighted least square fit using the variable representing a smaller error as an explanatory variable**

(i) Plot size-classified particle concentrations as a function of time and retrieve the appearance time for a given particle size at a time when the concentration is 50% of the maximum concentration[166].

(ii) After retrieving the size-dependent appearance times, apply a linear regression model, for example, a weighted least square fit, to appearance time versus particle diameter data (for other options, see Mikkonen et al.[194]), and calculate both the GR and error estimate directly based on the fit and fit uncertainty.

(B) **Total least squares or geometric mean regression**

▲ **CRITICAL STEP** The error in GR is determined using Monte Carlo simulation (or some other numerical method[195,196]).

(i) Assume normally distributed uncertainty that includes random and systematic errors in the measured particle concentration and particle diameter on the basis of instrument performance and reproduce 10,000 datasets for which the values are randomly picked from the estimated distribution around each data point.

(ii) Calculate the GR for all reproduced datasets.

(iii) Obtain the GR as the median value with uncertainty as ±1 s.d. For the example calculations, see the Anticipated results section and Fig. 3.

9 Report the value of GR with one significant figure if the error is >20% and with two significant figures if the error is <20%.

10 Determine the error in the formation rate using the Monte Carlo method. Reproduce the formation rate 10,000 times at the plateau value, from which formation rate is normally determined. First, as the detected particle number concentration above a given cutoff diameter depends on the cutoff diameter (‘Equipment setup’ section), estimate the relation between the cutoff diameter and detected particle concentration. Thereafter, assume independent uncertainties for the cutoff, N, k_{dil}, k_{wall}, and k_{coag}, which are normally distributed and include both random and systematic errors. Typically, in chamber experiments, the uncertainty in k_{dil} can be estimated from the dilution flow rate, the uncertainty in k_{wall} can be estimated from a decay experiment to which the decay rate can be fitted, and the uncertainty in k_{coag} is estimated assuming 10% error in the size distribution. The Monte Carlo run should be constructed so that the first cutoff diameter is selected from the cutoff distribution, which determines N, and for that N the uncertainty is normally distributed and selected randomly. If the size distribution is obtained from two or more instruments, the uncertainties in cutoff and N should be estimated for each instrument. Then run a Monte Carlo simulation and obtain J_{dp} as the median value with uncertainty as ±1 s.d. For the example calculations, see the Anticipated results and Fig. 2b.

11 After determining the error in the formation rate, report the value of the formation rate with one significant figure if the error is >20% and two significant figures if the error is <20%.

12 (Optional) Determine the importance of charge in NPF by comparing the ion formation rate (determined from measured ion size distributions[114]) to the total J_{dp} value. When calculating the formation rate of charged particles, additional terms need to be added to Eq. 9 in order to account for the loss of ions due to ion–ion recombination (S_{rec}) and the production of ions by the charging of neutral particles (S_{att})[197]. As calculating recombination and charging between all sizes is rather complicated, we recommend calculating charged formation rates from ion size distribution in a size

bin between diameters d_p and the upper diameter d_u. For this reason, a term describing the growth of ions out of the studied size bin (S_{growth}) also needs to be included when calculating the ion formation rate. The equation for calculating the ion formation rate for positive (superscript +) and negative ions (superscript −) is as follows:

$$J_{dp}^{\pm} = \frac{dN_{dp-du}^{\pm}}{dt} + S_{dil} + S_{wall} + S_{growth} + S_{coag} + S_{rec} - S_{att}\,[\mathrm{cm^{-3}s^{-1}}] \quad (11)$$

$\frac{dN_{dp-du}^{\pm}}{dt}$ is the time derivative of the ion concentration in a certain size bin, measured with a NAIS or some other ion instrument. The terms describing the loss of ions due to dilution (S_{dil}), deposition on chamber walls (S_{wall}) and coagulation (S_{coag}) are calculated as described in Steps 3–5, but instead of calculating them for all the particles larger than a certain threshold size, they are calculated for ions in a size bin between d_p and d_u.

The equation for calculating the loss of ions due to growth out of the studied size bin is as follows:

$$S_{growth} = \frac{N}{(d_u - d_p)} \times \mathrm{GR} \quad (12)$$

where GR is the growth rate of ions out of the size bin, which can be determined from the ion size distribution (see Step 1).

The equation for calculating the loss rate of ions due to ion–ion recombination is as follows:

$$S_{rec} = \alpha N_{dp-du}^{\pm} N_{<dp}^{\mp} \quad (13)$$

α is the ion–ion recombination coefficient, for which the constant value of 1.6×10^{-6} cm^3 s^{-1} is usually assumed[198]. Note that the recombination coefficient depends on both the size and the chemical composition of ions, as well as on environmental conditions such as temperature and RH[199].

The equation for calculating the production rate of ions due to charging of neutral particles is as follows:

$$S_{att=}\chi N_{dp-du} N_{<dp}^{\pm} \quad (14)$$

χ is the ion–aerosol attachment coefficient which, similar to the recombination coefficient, depends on the particle size and environmental conditions. χ is usually assumed to equal 0.01×10^{-6} cm^3 s^{-1} (ref. [200]).

13 (Optional) If a high-voltage field is available inside the chamber to remove all ions, calculate the contribution of charged species to the total particle number concentration. When the high-voltage field is off, the total J_{dp} value consists of both neutral and charged particles ($J_{tot} = J_n + J^{\pm} + J_{rec}$). The neutral formation rate (J_n) can be determined from the time when the high-voltage field is on and all particles are produced by neutral processes. The formation rate resulting from charged particles ($J^{\pm} + J_{rec}$) involves the naturally charged ions and those that have lost their charge due to recombination. These two contributions cannot be distinguished using this method. The importance of ion processes can thus be assessed by comparing the total formation rates in these two cases. This method was introduced by Kirkby et al.[54] for the CLOUD chamber.

14 (Optional) If a high-voltage field is available and you are using an ion trap, calculate the formation rate of neutral particles due to recombination, J_{rec}, using the following equation:

$$J_{rec} = J_{tot} - J_n - J^{\pm} \quad (15)$$

The total particle formation rate (J_{tot}) consists of both neutral and charged parts and is calculated with the high-voltage field turned off, whereas the neutral formation rate (J_n) can be determined from the time when the high-voltage field is on and all particles are produced by neutral processes (see Steps 6 and 7). $J^{\pm}$ is the ion formation rate, which is the difference between J_{tot} and $J_{n,tot}$ acquired by using an ion trap in front of the particle measurement instrument (Step 7; Eq. 10).

Troubleshooting

Troubleshooting advice can be found in Table 6.

Table 6 | Troubleshooting table

Step	Problem	Solution
1	No NPF is observed	Check that precursor gas injection works and the gas concentration in the chamber is what you expect (when a new gas is introduced into the chamber, there could be a delay in the increase of the gas phase concentration due to saturation of walls and inlet lines)
		Check the performance of the particle-counting instruments. If everything works, the precursor vapor concentration might be too low for NPF
	Unexpected particle formation/particle burst is detected	Check that chamber mixing works (avoid introducing reactants through a shared inlet) and that there are no fluctuations in any of the flows or chamber conditions
		Check for contamination from the gas injection system, chamber wall or backflow from the sampling instruments
		Check that the precursor concentration is what you expect
		Check that there are no leaks in your instruments
1,6	Particle formation stops unexpectedly	Check that there is no interruption or drop in the gas injection and that the measured gas concentrations are stable
		Check that the measurement instruments are working correctly
		The sink from growing particles might be too high to completely suppress particle formation and growth
		A drop in the J_{dp} value can sometimes be seen at the start of an experiment when the gas and particle concentrations first peak, and then a steady-state value is reached when production and losses stabilize
1,2(A,B,C),6	The size distribution plot does not look like a 'banana' or multiple 'bananas' are detected	Owing to different dynamics (see Introduction), size distribution during particle formation might look different in the chamber than in the atmosphere. Particle formation usually continues as long as the precursor concentration is high enough and the particle sink is low enough, so there is a threshold at which the first-formed particles grow, and continuous production and growth of particles occurs thereafter. Multiple bananas can be observed if there is fluctuation in conditions or the sink becomes lower during the experiment
2(A,B,C)	Particles form, but they do not grow past a few nanometers	There could be an insufficient amount of precursor vapors capable of growing the particles, or the growth is very slow in comparison to the loss rates and dilution lifetime of the particles in the chamber
		Calculate the expected GR on the basis of vapor concentrations
		Check that the instruments measuring growth (e.g., SMPSs) are able to detect the growing particles (losses in mobility spectrometers are often very high for the smallest particles and, if the particle concentration in the chamber is low, the growing particles might not be detected at all)
2(A,B)	Particle GR determined using maximum concentration or appearance time method appears to be negative	It is possible that the slope of the linear fit to $d_{p,mean,i}$ versus $t_{max,i}/t_{app50,i}/t_{app,i}$ data is negative. This can be caused by very fast particle growth, in which case the time difference between different sizes is too small to be detected. Try a different method or a wider size range. Negative GR can also be caused by errors in the measured particle size distribution
2,6	Results (e.g., J or GR at a certain gas concentration) do not match the values reported in previous studies (within error estimates)	Check the performance of the instruments (both precursor gas and particle measurements) and their calibration. If J or GR is lower than expected, there could be losses that are not accounted for (see 'Equipment setup' in the Materials section for inlet line losses) or the gas concentration may have been overestimated
		Check for contamination or some other unaccounted for precursor vapor; the particle losses could be overestimated or the gas concentration could be underestimated
6	J is not increasing with increased precursor vapor concentration	Check that the particle-counting instruments are detecting particles correctly (e.g., maximum detectable concentration is not exceeded, there is enough working fluid).
		If no technical problems are detected, J might be saturated with respect to this variable or not affected by it

Timing

Step 1, pre-injection measurement of chamber background: 30 min; injection of precursors: 5 min
Step 2, determination of the GR: 12 min to several hours, depending on the amount of precursors, the GR, the aimed-for maximum diameter and the chamber dilution lifetime. Typical GRs at atmospheric conditions and concentrations vary from <1 nm/h to several tens of nanometers per hour.
Steps 3–5, determination of particle losses: 12 min to several hours, depending on the concentration of precursors that results in the formation of particles in the size range of interest
Step 6, determination of formation rate: 12 min to several hours; see timing for Steps 1–5
Step 7, determination of ion nucleation rate: 12 min to several hours; see timing for Steps 1–5
Steps 8 and 9, determination of error on GR: 12 min to several hours; see timing for Step 2
Steps 10 and 11, determination of error on formation rate: 12 min to several hours; see timing for Steps 1–5
Steps 12–14, determination of ion nucleation rate (alternative methods): 12 min to several hours; see timing for Steps 1–5

Anticipated results

An example of an NPF experiment is shown in Fig. 2a. A surface plot exhibiting a banana-shaped NPF event represents the anticipated time evolution of particle size distribution in an experiment in which particles constantly form until the gas injection or oxidation is stopped and the gases and particles are left to decay. To determine J_{dp}, the experiment should be stopped only when a steady-state value is reached and kept for a long enough time to allow for averaging over a suitable period (e.g., 12 min, depending on the instrument's time resolutions); see Fig. 3b. For measuring GR, the experiment should be continued until the particle size distribution has reached the sizes of interest. If the experiment is stopped too early, particles will not reach large enough sizes to allow for the calculation of growth. An example of the calculation of particle formation is shown in Fig. 2b. The formation rate usually increases rapidly in the beginning of the experiment when gas concentrations in the chamber increase as the experiment is started (usually by turning on UV lights or by starting gas injection). To obtain a single formation rate value per experiment (representing a specific set of conditions), the formation rate can be averaged over the period with steady chamber conditions (steady state), demonstrated by 'steady' in Fig. 2. In our example, the anticipated GR $= 2.0 \pm 0.4$ nm h^{-1}, and the anticipated $J_{1.5} = 2.0 + 0.4$ cm^{-3} s^{-1}, as shown in Figs. 2b and 3c, respectively.

Reporting Summary

Further information on research design is available in the Nature Research Reporting Summary linked to this article.

References

1. Spracklen, D. V. et al. The contribution of boundary layer nucleation events to total particle concentrations on regional and global scales. *Atmos. Chem. Phys.* **6**, 5631–5648 (2006).
2. Yu, F. et al. Spatial distributions of particle number concentrations in the global troposphere: Simulations, observations, and implications for nucleation mechanisms. *J. Geophy. Res.* **115**, D17205 (2010).
3. Spracklen, D. V. et al. Contribution of particle formation to global cloud condensation nuclei concentrations. *Geophy. Res. Lett.* **35**, L06808 (2008).
4. Kerminen, V. M. et al. Cloud condensation nuclei production associated with atmospheric nucleation: a synthesis based on existing literature and new results. *Atmos. Chem. Phys.* **12**, 12037–12059 (2012).
5. Guo, S. et al. Elucidating severe urban haze formation in China. *Proc. Natl Acad. Sci. USA* **111**, 17373–17378 (2014).
6. Jiang, J. K. et al. First measurements of neutral atmospheric cluster and 1-2 nm particle number size distributions during nucleation events. *Aerosol Sci. Technol.* **45**, ii–v (2011).
7. Kulmala, M. et al. Direct observations of atmospheric aerosol nucleation. *Science* **339**, 943–946 (2013).
8. Zhang, R., Khalizov, A., Wang, L., Hu, M. & Xu, W. Nucleation and growth of nanoparticles in the atmosphere. *Chem. Rev.* **112**, 1957–2011 (2011).
9. Kerminen, V.-M. et al. Atmospheric new particle formation and growth: review of field observations. *Environ. Res. Lett.* **13**, 103003 (2018).
10. Chu, B. et al. Atmospheric new particle formation in China. *Atmos. Chem. Phys.* **19**, 115–138 (2019).
11. Akimoto, H., Sakamaki, F., Hoshino, M., Inoue, G. & Okuda, M. Photochemical ozone formation in propylene-nitrogen oxide-dry air system. *Environ. Sci.* **13**, 53–58 (1979).

12. Alfarra, M. R. et al. A mass spectrometric study of secondary organic aerosols formed from the photooxidation of anthropogenic and biogenic precursors in a reaction chamber. *Atmos. Chem. Phys.* **6**, 5279–5293 (2006).
13. Atkinson, R., Carter, W. P. L., Darnall, K. R., Winer, A. M. & Pitts Jr., J. N. A smog chamber and modeling study of the gas phase NOx–air photooxidation of toluene and the cresols. **12**, 779-836 (1980).
14. Barsanti, K. C., McMurry, P. H. & Smith, J. N. The potential contribution of organic salts to new particle growth. *Atmos. Chem. Phys.* **9**, 2949–2957 (2009).
15. Becker, K. H. *Overview on the Development of Chambers for the Study of Atmospheric Chemical Processes* (Springer Netherlands, 2006).
16. Behnke, W., Holländer, W., Koch, W., Nolting, F. & Zetzsch, C. A smog chamber for studies of the photochemical degradation of chemicals in the presence of aerosols. *Atmos. Environ.* **22**, 1113–1120 (1988).
17. Bruns, E. A. et al. Inter-comparison of laboratory smog chamber and flow reactor systems on organic aerosol yield and composition. *Atmos. Meas. Technol.* **8**, 2315–2332 (2015).
18. Böge, O., Miao, Y., Plewka, A. & Herrmann, H. Formation of secondary organic particle phase compounds from isoprene gas-phase oxidation products: an aerosol chamber and field study. *Atmos. Environ.* **40**, 2501–2509 (2006).
19. Carter, W. P. L., Atkinson, R., Winer, A. M. & Pitts, J. N. Jr. Experimental investigation of chamber-dependent radical sources. *Int. J. Chem. Kinet.* **14**, 1071–1103 (1982).
20. Carter, W. P. L. et al. A new environmental chamber for evaluation of gas-phase chemical mechanisms and secondary aerosol formation. *Atmos. Environ.* **39**, 7768–7788 (2005).
21. Dodge, M. C. Chemical oxidant mechanisms for air quality modeling: critical review. *Atmos. Environ.* **34**, 2103–2130 (2000).
22. Donahue, N. M. et al. Aging of biogenic secondary organic aerosol via gas-phase OH radical reactions. *Proc. Natl Acad. Sci. USA* **109**, 13503–13508 (2012).
23. Ehn, M. et al. A large source of low-volatility secondary organic aerosol. *Nature* **506**, 476–479 (2014).
24. Hallquist, M. et al. The formation, properties and impact of secondary organic aerosol: current and emerging issues. *Atmos. Chem. Phys.* **9**, 5155–5236 (2009).
25. Hess, G. D., Carnovale, F., Cope, M. E. & Johnson, G. M. The evaluation of some photochemical smog reaction mechanisms—I. Temperature and initial composition effects. *Atmos. Environ. A Gen. Top.* **26**, 625–641 (1992).
26. Hoffmann, T. et al. Formation of organic aerosols from the oxidation of biogenic hydrocarbons. *J. Atmos. Chem.* **26**, 189–222 (1997).
27. Jeffries, H., Kamens, R., Sexron, K. & Gerhardt, A. Outdoor smog chamber experiments to test photochemical models. Final report May 78–May 81 (North Carolina University at Chapel Hill School of Public Health, 1982).
28. Jimenez, J. L. et al. Evolution of organic aerosols in the atmosphere. *Science* **326**, 1525–1529 (2009).
29. Kalberer, M., Sax, M. & Samburova, V. Molecular size evolution of oligomers in organic aerosols collected in urban atmospheres and generated in a smog chamber. *Environ. Sci. Technol.* **40**, 5917–5922 (2006).
30. Kroll, J. H., Ng, N. L., Murphy, S. M., Flagan, R. C. & Seinfeld, J. H. Secondary organic aerosol formation from isoprene photooxidation under high-NOx conditions. *Geophys. Res. Lett.* **32**, L18808 (2005).
31. Kroll, J. H. et al. Chamber studies of secondary organic aerosol growth by reactive uptake of simple carbonyl compounds. *J. Geophys. Res.* **110**, D23207 (2005).
32. Leskinen, A. P., Kulmala, M. & Lehtinen, K. E. J. Growth of nucleation mode particles: source rates of condensable vapour in a smog chamber. *Atmos. Environ.* **42**, 7405–7411 (2008).
33. Martín-Reviejo, M. & Wirtz, K. Is benzene a precursor for secondary organic aerosol? *Environ. Sci. Technol.* **39**, 1045–1054 (2005).
34. McFiggans, G. et al. Secondary organic aerosol reduced by mixture of atmospheric vapours. *Nature* **565**, 587–593 (2019).
35. McMurry, P. H. Photochemical aerosol formation from SO2: a theoretical analysis of smog chamber data. *J. Colloid Interf. Sci.* **78**, 513–527 (1980).
36. Ng, N. L. et al. Secondary organic aerosol formation from *m*-xylene, toluene, and benzene. *Atmos. Chem. Phys.* **7**, 3909–3922 (2007).
37. Nordin, E. Z. et al. Secondary organic aerosol formation from idling gasoline passenger vehicle emissions investigated in a smog chamber. *Atmos. Chem. Phys.* **13**, 6101–6116 (2013).
38. O'Dowd, C. D. et al. Marine aerosol formation from biogenic iodine emissions. *Nature* **417**, 632 (2002).
39. Odum, J. R. et al. Gas/particle partitioning and secondary organic aerosol yields. *Environ. Sci. Technol.* **30**, 2580–2585 (1996).
40. Pandis, S. N., Paulson, S. E., Seinfeld, J. H. & Flagan, R. C. Aerosol formation in the photooxidation of isoprene and β-pinene. *Atmos. Environ. A Gen. Top.* **25**, 997–1008 (1991).
41. Platt, S. M. et al. Secondary organic aerosol formation from gasoline vehicle emissions in a new mobile environmental reaction chamber. *Atmos. Chem. Phys.* **13**, 9141–9158 (2013).
42. Riva, M. et al. Chemical transformations in monoterpene-derived organic aerosol enhanced by inorganic composition. *npj Clim. Atmos. Sci.* **2**, 2 (2019).
43. Simonaitis, R., Meagher, J. F. & Bailey, E. M. Evaluation of the condensed carbon bond (CB-IV) mechanism against smog chamber data at low VOC and NOx concentrations. *Atmos. Environ.* **31**, 27–43 (1997).

44. Smith, J. N. et al. Observations of aminium salts in atmospheric nanoparticles and possible climatic implications. *Proc. Natl Acad. Sci. USA* **107**, 6634–6639 (2010).
45. Tritscher, T. et al. Volatility and hygroscopicity of aging secondary organic aerosol in a smog chamber. *Atmos. Chem. Phys.* **11**, 11477–11496 (2011).
46. Wang, X. et al. Design and characterization of a smog chamber for studying gas-phase chemical mechanisms and aerosol formation. *Atmos. Meas. Technol.* **7**, 301–313 (2014).
47. Weitkamp, E. A., Sage, A. M., Pierce, J. R., Donahue, N. M. & Robinson, A. L. Organic aerosol formation from photochemical oxidation of diesel exhaust in a smog chamber. *Environ. Sci. Technol.* **41**, 6969–6975 (2007).
48. Zhang, X. et al. Influence of vapor wall loss in laboratory chambers on yields of secondary organic aerosol. *Proc. Natl Acad. Sci. USA* **111**, 5802–7 (2014).
49. Zhao, J. et al. Observation of neutral sulfuric acid-amine containing clusters in laboratory and ambient measurements. *Atmos. Chem. Phys.* **11**, 10823–10836 (2011).
50. Garnier, J. P. & Mirabel, P. Experimental study of nucleation in binary mixtures: the methanol–ethanol, methanol-n-propanol, and ethanol-n-propanol systems. *J. Chem. Phys.* **77**, 2035–2037 (1982).
51. Viisanen, Y., Kulmala, M. & Laaksonen, A. Experiments on gas–liquid nucleation of sulfuric acid and water. *J. Chem. Phys.* **107**, 920–926 (1997).
52. Ball, S., Hanson, D., Eisele, F. & McMurry, P. Laboratory studies of particle nucleation: initial results for H_2SO_4, H_2O, and NH_3 vapors. *J. Geophys. Res-Atmos.* **104**, 23709–23718 (1999).
53. Mirabel, P. & Clavelin, J. L. Experimental study of nucleation in binary mixtures: the nitric acid–water and sulfuric acid–water systems. *J. Chem. Phys.* **68**, 5020–5027 (1978).
54. Kirkby, J. et al. Role of sulphuric acid, ammonia and galactic cosmic rays in atmospheric aerosol nucleation. *Nature* **476**, 429–433 (2011).
55. Dawson, M. L. et al. Simplified mechanism for new particle formation from methanesulfonic acid, amines, and water via experiments and ab initio calculations. *Proc. Natl Acad. Sci. USA* **109**, 18719–18724 (2012).
56. Ezell, M. et al. A new aerosol flow system for photochemical and thermal studies of tropospheric aerosols. *Aerosol Sci. Technol.* **44**, 329–338 (2010).
57. Jimenez, J. L. et al. New particle formation from photooxidation of diiodomethane (CH2I2). *J. Geophys. Res.* **108**, 4318 (2003).
58. Zhang, R. et al. Atmospheric new particle formation enhanced by organic acids. *Science* **304**, 1487–1490 (2004).
59. Berndt, T., Böge, O., Stratmann, F., Heintzenberg, J. & Kulmala, M. Rapid formation of sulfuric acid particles at near-atmospheric conditions. *Science* **307**, 698–700 (2005).
60. Berndt, T., Böge, O. & Stratmann, F. Formation of atmospheric H_2SO_4/H_2O particles in the absence of organics: a laboratory study. *Geophys. Res. Lett.* **33**, L15817 (2006).
61. Benson, D. R., Young, L.-H., Kameel, F. R. & Lee, S.-H. Laboratory-measured nucleation rates of sulfuric acid and water binary homogeneous nucleation from the $SO_2 + OH$ reaction. *Geophys. Res. Lett.* **35**, L11801 (2008).
62. Berndt, T. et al. SO_2 oxidation products other than H_2SO_4 as a trigger of new particle formation. Part 1: laboratory investigations. *Atmos. Chem. Phys.* **8**, 6365–6374 (2008).
63. Young, L. H. et al. Laboratory studies of H_2SO_4/H_2O binary homogeneous nucleation from the SO_2+OH reaction: evaluation of the experimental setup and preliminary results. *Atmos. Chem. Phys.* **8**, 4997–5016 (2008).
64. Berndt, T. et al. Laboratory study on new particle formation from the reaction OH + SO_2: influence of experimental conditions, H_2O vapour, NH_3 and the amine tert-butylamine on the overall process. *Atmos. Chem. Phys.* **10**, 7101–7116 (2010).
65. Brus, D., Hyvärinen, A. P., Viisanen, Y., Kulmala, M. & Lihavainen, H. Homogeneous nucleation of sulfuric acid and water mixture: experimental setup and first results. *Atmos. Chem. Phys.* **10**, 2631–2641 (2010).
66. Duplissy, J. et al. Results from the CERN pilot CLOUD experiment. *Atmos. Chem. Phys.* **10**, 1635–1647 (2010).
67. Sipilä, M. et al. The role of sulfuric acid in atmospheric nucleation. *Science* **327**, 1243–1246 (2010).
68. Wang, L. et al. Atmospheric nanoparticles formed from heterogeneous reactions of organics. *Nat. Geosci.* **3**, 238 (2010).
69. Brus, D. et al. Homogenous nucleation of sulfuric acid and water at close to atmospherically relevant conditions. *Atmos. Chem. Phys.* **11**, 5277–5287 (2011).
70. Kiendler-Scharr, A. et al. New particle formation in forests inhibited by isoprene emissions. *Nature* **461**, 381–384 (2009).
71. Benson, D. R., Yu, J. H., Markovich, A. & Lee, S. H. Ternary homogeneous nucleation of H2SO4, NH3, and H2O under conditions relevant to the lower troposphere. *Atmos. Chem. Phys.* **11**, 4755–4766 (2011).
72. Yu, H., McGraw, R. & Lee, S.-H. Effects of amines on formation of sub-3 nm particles and their subsequent growth. *Geophys. Res. Lett.* **39**, L02807 (2012).
73. Zollner, J. H. et al. Sulfuric acid nucleation: power dependencies, variation with relative humidity, and effect of bases. *Atmos. Chem. Phys.* **12**, 4399–4411 (2012).
74. Almeida, J. et al. Molecular understanding of sulphuric acid-amine particle nucleation in the atmosphere. *Nature* **502**, 359–363 (2013).

75. Schobesberger, S. et al. Molecular understanding of atmospheric particle formation from sulfuric acid and large oxidized organic molecules. *Proc. Natl Acad. Sci. USA* **110**, 17223–17228 (2013).
76. Jen, C. N., McMurry, P. H. & Hanson, D. R. Stabilization of sulfuric acid dimers by ammonia, methylamine, dimethylamine, and trimethylamine. *J. Geophys. Res. Atmos.* **119**, 7502–7514 (2014).
77. Riccobono, F. et al. Oxidation products of biogenic emissions contribute to nucleation of atmospheric particles. *Science* **344**, 717–721 (2014).
78. Glasoe, W. A. et al. Sulfuric acid nucleation: an experimental study of the effect of seven bases. *J. Geophys. Res. Atmos.* **120**, 1933–1950 (2015).
79. Chen, H. et al. New particle formation and growth from methanesulfonic acid, trimethylamine and water. *Phys. Chem. Chem. Phys.* **17**, 13699–13709 (2015).
80. Chen, H., Varner, M. E., Gerber, R. B. & Finlayson-Pitts, B. J. Reactions of methanesulfonic acid with amines and ammonia as a source of new particles in air. *J. Phys. Chem. B* **120**, 1526–1536 (2016).
81. Jen, C. N., Bachman, R., Zhao, J., McMurry, P. H. & Hanson, D. R. Diamine-sulfuric acid reactions are a potent source of new particle formation. *Geophys. Res. Lett.* **43**, 867–873 (2016).
82. Lehtipalo, K. et al. The effect of acid-base clustering and ions on the growth of atmospheric nano-particles. *Nat. Commun.* **7**, 11594 (2016).
83. Yu, H. et al. Laboratory observations of temperature and humidity dependencies of nucleation and growth rates of sub-3 nm particles. *J. Geophys. Res. Atmos.* **122**, 1919–1929 (2017).
84. Chen, H. & Finlayson-Pitts, B. J. New particle formation from methanesulfonic acid and amines/ammonia as a function of temperature. *Environ. Sci. Technol.* **51**, 243–252 (2017).
85. Tröstl, J. et al. The role of low-volatility organic compounds in initial particle growth in the atmosphere. *Nature* **533**, 527–531 (2016).
86. Dal Maso, M. et al. A chamber study of the influence of boreal BVOC emissions and sulfuric acid on nanoparticle formation rates at ambient concentrations. *Atmos. Chem. Phys.* **16**, 1955–1970 (2016).
87. Boulon, J. et al. Sub-3 nm particles detection in a large photoreactor background: possible implications for new particles formation studies in a smog chamber. *Aerosol Sci. Technol.* **47**, 153–157 (2013).
88. Wang, J. et al. Design of a new multi-phase experimental simulation chamber for atmospheric photosmog, aerosol and cloud chemistry research. *Atmos. Meas. Technol.* **4**, 2465 (2011).
89. Pichelstorfer, L. et al. Resolving nanoparticle growth mechanisms from size- and time-dependent growth rate analysis. *Atmos. Chem. Phys.* **18**, 1307–1323 (2018).
90. Kürten, A. et al. New particle formation in the sulfuric acid-dimethylamine-water system: reevaluation of CLOUD chamber measurements and comparison to an aerosol nucleation and growth model. *Atmos. Chem. Phys.* **18**, 845–863 (2018).
91. Hao, L. Q. et al. New particle formation from the oxidation of direct emissions of pine seedlings. *Atmos. Chem. Phys.* **9**, 8121–8137 (2009).
92. Joutsensaari, J. et al. Nanoparticle formation by ozonolysis of inducible plant volatiles. *Atmos. Chem. Phys.* **5**, 1489–1495 (2005).
93. Paulsen, D. et al. Secondary organic aerosol formation by irradiation of 1, 3, 5-trimethylbenzene−NOx −H_2O in a new reaction chamber for atmospheric chemistry and physics. *Environ. Sci. Technol.* **39**, 2668–2678 (2005).
94. Metzger, A. et al. Evidence for the role of organics in aerosol particle formation under atmospheric conditions. *Proc. Natl Acad. Sci. USA* **107**, 6646–6651 (2010).
95. Riccobono, F. et al. Contribution of sulfuric acid and oxidized organic compounds to particle formation and growth. *Atmos. Chem. Phys.* **12**, 9427–9439 (2012).
96. Duplissy, J. et al. Effect of ions on sulfuric acid-water binary particle formation: 2. Experimental data and comparison with QC-normalized classical nucleation theory. *J. Geophys. Res. Atmos.* **121**, 1752–1775 (2016).
97. Wagner, R. et al. The role of ions in new particle formation in the CLOUD chamber. *Atmos. Chem. Phys.* **17**, 15181–15197 (2017).
98. Kirkby, J. et al. Ion-induced nucleation of pure biogenic particles. *Nature* **533**, 521–526 (2016).
99. Smith, J. N., Moore, K. F., McMurry, P. H. & Eisele, F. L. Atmospheric measurements of sub-20 nm diameter particle chemical composition by thermal desorption chemical ionization mass spectrometry. *Aerosol Sci. Technol.* **38**, 100–110 (2004).
100. Smith, J. N., Winkler, P. M., Zhao, J. & McMurry, P. H. Exploring the role of organics in atmospheric new particle formation with chemical ionization mass spectrometry. *Abstr. Pap. Am. Chem. Soc.* **242**, ENVR 428 (2011).
101. Smith, J. N. & Rathbone, G. J. Carboxylic acid characterization in nanoparticles by thermal desorption chemical ionization mass spectrometry. *Int. J. Mass. Spectrom.* **274**, 8–13 (2008).
102. Lehtipalo, K. et al. Multicomponent new particle formation from sulfuric acid, ammonia, and biogenic vapors. *Sci. Adv.* **4**, eaau5363 (2018).
103. Dunne, E. M. et al. Global atmospheric particle formation from CERN CLOUD measurements. *Science* **354**, 1119–1124 (2016).
104. Gordon, H. et al. Causes and importance of new particle formation in the present-day and preindustrial atmospheres. *J. Geophys. Res. Atmos.* **122**, 8739–8760 (2017).
105. Gordon, H. et al. Reduced anthropogenic aerosol radiative forcing caused by biogenic new particle formation. *Proc. Natl Acad. Sci. USA* **113**, 12053–12058 (2016).

106. Cziczo, D. J. *et al*. Ice nucleation by surrogates of Martian mineral dust: what can we learn about Mars without leaving Earth? **118**, 1945-1954 (2013).
107. Berndt, T. et al. Enhancement of atmospheric H_2SO_4/H_2O nucleation: organic oxidation products versus amines. *Atmos. Chem. Phys.* **14**, 751–764 (2014).
108. McMurry, P. H. & Grosjean, D. Gas and aerosol wall losses in Teflon film smog chambers. *Environ. Sci. Technol.* **19**, 1176–1182 (1985).
109. Liu, D.-L. in *Developments in Surface Contamination and Cleaning* (eds Kohli, R. & Mittal, K. L.) 1–56 (William Andrew Publishing, 2010).
110. Schwantes, R. H. et al. in *Advances in Atmospheric Chemistry* 1–93 (World Scientific, 2017).
111. Neitola, K. et al. Total sulfate vs. sulfuric acid monomer concenterations in nucleation studies. *Atmos. Chem. Phys.* **15**, 3429–3443 (2015).
112. Stolzenburg, D. et al. Rapid growth of organic aerosol nanoparticles over a wide tropospheric temperature range. *Proc. Natl Acad. Sci. USA* **115**, 9122–9127 (2018).
113. Wildt, J. et al. Suppression of new particle formation from monoterpene oxidation by NO_x. *Atmos. Chem. Phys.* **14**, 2789–2804 (2014).
114. Kulmala, M. et al. Measurement of the nucleation of atmospheric aerosol particles. *Nat. Protoc.* **7**, 1651–1667 (2012).
115. Kerminen, V. M. & Kulmala, M. Analytical formulae connecting the "real" and the "apparent" nucleation rate and the nuclei number concentration for atmospheric nucleation events. *J. Aerosol Sci.* **33**, 609–622 (2002).
116. Lehtinen, K. E. J., Dal Maso, M., Kulmala, M. & Kerminen, V. M. Estimating nucleation rates from apparent particle formation rates and vice versa: revised formulation of the Kerminen-Kulmala equation. *J. Aerosol Sci.* **38**, 988–994 (2007).
117. Korhonen, H., Kerminen, V.-M., Kokkola, H. & Lehtinen, K. E. J. Estimating atmospheric nucleation rates from size distribution measurements: analytical equations for the case of size dependent growth rates. *J. Aerosol Sci.* **69**, 13–20 (2014).
118. Kürten, A., Williamson, C., Almeida, J., Kirkby, J. & Curtius, J. On the derivation of particle nucleation rates from experimental formation rates. *Atmos. Chem. Phys.* **15**, 4063–4075 (2015).
119. Brines, M. et al. Traffic and nucleation events as main sources of ultrafine particles in high-insolation developed world cities. *Atmos. Chem. Phys.* **15**, 5929–5945 (2015).
120. Cai, R. et al. Estimating the influence of transport on aerosol size distributions during new particle formation events. *Atmos. Chem. Phys.* **18**, 16587–16599 (2018).
121. Dada, L. et al. Refined classification and characterization of atmospheric new-particle formation events using air ions. *Atmos. Chem. Phys.* **18**, 17883–17893 (2018).
122. Leino, K. et al. Vertical profiles of sub-3 nm particles over the boreal forest. *Atmos. Chem. Phys.* **19**, 4127–4138 (2019).
123. Kerminen, V. M., Lehtinen, K. E. J., Anttila, T. & Kulmala, M. Dynamics of atmospheric nucleation mode particles: a timescale analysis. *Tellus B* **56**, 135–146 (2004).
124. Cai, R., Mirme, S., Jiang, J. & Kangasluoma, J. Parameters to determine the optimum performance of electrical mobility spectrometers for measurement of particle size distributions down to the cluster size. *J. Aerosol Sci.* **127**, 102–115 (2018).
125. Mordas, G. et al. Design and performance characteristics of a condensation particle counter UF-02proto. *Boreal Environ. Res.* **10**, 543–552 (2005).
126. Collins, A. M., Dick, W. D. & Romay, F. J. A new coincidence correction method for condensation particle counters. *Aerosol Sci. Technol.* **47**, 177–182 (2013).
127. Kebabian, P. L., Herndon, S. C. & Freedman, A. Detection of nitrogen dioxide by cavity attenuated phase shift spectroscopy. *Anal. Chem.* **77**, 724–728 (2005).
128. Rohrer, F. & Brüning, D. Surface NO and NO_2 mixing ratios measured between 30 N and 30 S in the Atlantic region. *J. Atmos. Chem.* **15**, 253–267 (1992).
129. Hansel, A. et al. Proton transfer reaction mass spectrometry: on-line trace gas analysis at the ppb level. *Int. J. Mass. Spectrom.* **149**, 609–619 (1995).
130. Blake, R. S., Monks, P. S. & Ellis, A. M. Proton-transfer reaction mass spectrometry. *Chem. Rev.* **109**, 861–896 (2009).
131. Yuan, B. et al. Proton-transfer-reaction mass spectrometry: applications in atmospheric sciences. *Chem. Rev.* **117**, 13187–13229 (2017).
132. Jokinen, T. et al. Atmospheric sulphuric acid and neutral cluster measurements using CI-APi-TOF. *Atmos. Chem. Phys.* **12**, 4117–4125 (2012).
133. Kürten, A., Rondo, L., Ehrhart, S. & Curtius, J. Calibration of a chemical ionization mass spectrometer for the measurement of gaseous sulfuric acid. *Phys. Chem. A* **116**, 6375–6386 (2012).
134. Heinritzi, M. et al. Characterization of the mass-dependent transmission efficiency of a CIMS. *Atmos. Meas. Technol.* **9**, 1449–1460 (2016).
135. Lee, B. H. et al. An iodide-adduct high-resolution time-of-flight chemical-ionization mass spectrometer: application to atmospheric inorganic and organic compounds. *Environ. Sci. Technol.* **48**, 6309–6317 (2014).
136. Brophy, P. & Farmer, D. K. Clustering, methodology, and mechanistic insights into acetate chemical ionization using high-resolution time-of-flight mass spectrometry. *Atmos. Meas. Technol.* **9**, 3969–3986 (2016).

137. Breitenlechner, M. et al. PTR3: an instrument for studying the lifecycle of reactive organic carbon in the atmosphere. *Anal. Chem.* **89**, 5824–5831 (2017).
138. Krechmer, J. et al. Evaluation of a new reagent-ion source and focusing ion–molecule reactor for use in proton-transfer-reaction mass spectrometry. *Anal. Chem.* **90**, 12011–12018 (2018).
139. Yao, L. et al. Detection of atmospheric gaseous amines and amides by a high-resolution time-of-flight chemical ionization mass spectrometer with protonated ethanol reagent ions. *Atmos. Chem. Phys.* **16**, 14527–14543 (2016).
140. Zheng, J. et al. Measurement of atmospheric amines and ammonia using the high resolution time-of-flight chemical ionization mass spectrometry. *Atmos. Environ.* **102**, 249–259 (2015).
141. Simon, M. et al. Detection of dimethylamine in the low pptv range using nitrate chemical ionization atmospheric pressure interface time-of-flight (CI-APi-TOF) mass spectrometry. *Atmos. Meas. Technol.* **9**, 2135–2145 (2016).
142. Praplan, A. P., Bianchi, F., Dommen, J. & Baltensperger, U. Dimethylamine and ammonia measurements with ion chromatography during the CLOUD4 campaign. *Atmos. Meas. Technol.* **5**, 2161–2167 (2012).
143. Junninen, H. et al. A high-resolution mass spectrometer to measure atmospheric ion composition. *Atmo. s. Meas. Technol.* **3**, 1039–1053 (2010).
144. Frege, C. et al. Influence of temperature on the molecular composition of ions and charged clusters during pure biogenic nucleation. *Atmos. Chem. Phys.* **18**, 65–79 (2018).
145. Bianchi, F. et al. The role of highly oxygenated molecules (HOMs) in determining the composition of ambient ions in the boreal forest. *Atmos. Chem. Phys.* **17**, 13819–13831 (2017).
146. Ehn, M. et al. Composition and temporal behavior of ambient ions in the boreal forest. *Atmos. Chem. Phys.* **10**, 8513–8530 (2010).
147. Loza, C. L. et al. Characterization of vapor wall loss in laboratory chambers. *Environ. Sci. Technol.* **44**, 5074–5078 (2010).
148. Brauers, T. et al. Investigation of the formaldehyde differential absorption cross section at high and low spectral resolution in the simulation chamber SAPHIR. *Atmos. Chem. Phys.* **7**, 3579–3586 (2007).
149. Sumner, A. L. *et al.* in *Dynamics of Mercury Pollution on Regional and Global Scales: Atmospheric Processes and Human Exposures Around the World* (eds Pirrone, N. & Mahaffey, K. R.) 193–212 (Springer, 2005).
150. Grieshop, A. P., Logue, J. M., Donahue, N. M. & Robinson, A. L. Laboratory investigation of photochemical oxidation of organic aerosol from wood fires 1: measurement and simulation of organic aerosol evolution. *Atmos. Chem. Phys.* **9**, 1263–1277 (2009).
151. Byrne, M. A., Goddard, A. J. H., Lange, C. & Roed, J. Stable tracer aerosol deposition measurements in a test chamber. *J. Aerosol Sci.* **26**, 645–653 (1995).
152. Presto, A. A., Gordon, T. D. & Robinson, A. L. Primary to secondary organic aerosol: evolution of organic emissions from mobile combustion sources. *Atmos. Chem. Phys.* **14**, 5015–5036 (2014).
153. Hunter, J. F., Carrasquillo, A. J., Daumit, K. E. & Kroll, J. H. Secondary organic aerosol formation from acyclic, monocyclic, and polycyclic alkanes. *Environ. Sci. Technol.* **48**, 10227–10234 (2014).
154. Chhabra, P. S., Flagan, R. C. & Seinfeld, J. H. Elemental analysis of chamber organic aerosol using an aerodyne high-resolution aerosol mass spectrometer. *Atmos. Chem. Phys.* **10**, 4111–4131 (2010).
155. Saathoff, H. et al. Temperature dependence of yields of secondary organic aerosols from the ozonolysis of α-pinene and limonene. *Atmos. Chem. Phys.* **9**, 1551–1577 (2009).
156. Ye, P. et al. Vapor wall loss of semi-volatile organic compounds in a Teflon chamber. *Aerosol Sci. Technol.* **50**, 822–834 (2016).
157. Carter, W. P. L., Heo, G., Cocker III, D. R. & Nakao, S. *SOA formation: chamber study and model development*. Final report to the California Air Resources Board, contract no. 08-326 https://intra.engr.ucr.edu/~carter/SAPRC/pmchrpt.pdf (2012).
158. Cocker, D. R., Flagan, R. C. & Seinfeld, J. H. State-of-the-art chamber facility for studying atmospheric aerosol chemistry. *Environ. Sci. Technol.* **35**, 2594–2601 (2001).
159. McMurry, P. H. & Rader, D. J. Aerosol wall losses in electrically charged chambers. *Aerosol Sci. Technol.* **4**, 249–268 (1985).
160. Bloss, C. et al. Development of a detailed chemical mechanism (MCMv3.1) for the atmospheric oxidation of aromatic hydrocarbons. *Atmos. Chem. Phys.* **5**, 641–664 (2005).
161. Saathoff, H. et al. The AIDA soot aerosol characterisation campaign 1999. *J. Aerosol Sci.* **34**, 1277–1296 (2003).
162. Kulkarni, P., Baron, P. A. & Willeke, K. *Aerosol Measurement: Principles, Techniques, and Applications* (Wiley, 2011).
163. Ezell, M. J. et al. A new aerosol flow system for photochemical and thermal studies of tropospheric aerosols. *Aerosol Sci. Technol.* **44**, 329–338 (2010).
164. Stratmann, F. et al. Laboratory studies and numerical simulations of cloud droplet formation under realistic supersaturation conditions. *J. Atmos. Ocean Technol.* **21**, 876–887 (2004).
165. Lehtinen, K. E. J. & Kulmala, M. A model for particle formation and growth in the atmosphere with molecular resolution in size. *Atmos. Chem. Phys.* **3**, 251–257 (2003).
166. Lehtipalo, K. et al. Methods for determining particle size distribution and growth rates between 1 and 3 nm using the Particle Size Magnifier. *Boreal Environ. Res.* **19**, 215–236 (2014).
167. Kuang, C. et al. Size and time-resolved growth rate measurements of 1 to 5 nm freshly formed atmospheric nuclei. *Atmos. Chem. Phys.* **12**, 3573–3589 (2012).

168. Lehtinen, K. E. J., Rannik, Ü., Petäjä, T., Kulmala, M. & Hari, P. Nucleation rate and vapor concentration estimations using a least squares aerosol dynamics method. *J. Geophys. Res. Atmos*. **109**, D21209 (2004).
169. Verheggen, B. & Mozurkewich, M. An inverse modeling procedure to determine particle growth and nucleation rates from measured aerosol size distributions. *Atmos. Chem. Phys.* **6**, 2927–2942 (2006).
170. Yli-Juuti, T. et al. Growth rates of nucleation mode particles in Hyytiälä during 2003–2009: variation with particle size, season, data analysis method and ambient conditions. *Atmos. Chem. Phys.* **11**, 12865–12886 (2011).
171. Leppä, J., Anttila, T., Kerminen, V. M., Kulmala, M. & Lehtinen, K. E. J. Atmospheric new particle formation: real and apparent growth of neutral and charged particles. *Atmos. Chem. Phys.* **11**, 4939–4955 (2011).
172. Li, C. & McMurry, P. H. Errors in nanoparticle growth rates inferred from measurements in chemically reacting aerosol systems. *Atmos. Chem. Phys.* **18**, 8979–8993 (2018).
173. Vanhanen, J. et al. Particle size magnifier for nano-CN detection. *Aerosol Sci. Technol.* **45**, 533–542 (2011).
174. Stolzenburg, M. R. & McMurry, P. H. An ultrafine aerosol condensation nucleus counter. *Aerosol Sci. Technol.* **14**, 48–65 (1991).
175. Hering, S. V. et al. Detection near 1-nm with a laminar-flow, water-based condensation particle counter. *Aerosol Sci. Technol.* **51**, 354-362 (2017).
176. Wimmer, D. et al. Performance of diethylene glycol-based particle counters in the sub-3 nm size range. *Atmos. Meas. Technol.* **6**, 1793–1804 (2013).
177. Wang, S. C. & Flagan, R. C. Scanning electrical mobility spectrometer. *Aerosol Sci. Technol.* **13**, 230–240 (1990).
178. Mirme, S. & Mirme, A. The mathematical principles and design of the NAIS—a spectrometer for the measurement of cluster ion and nanometer aerosol size distributions. *Atmos. Meas. Technol.* **6**, 1061–1071 (2013).
179. Stolzenburg, D., Steiner, G. & Winkler, P. M. A DMA-train for precision measurement of sub-10 nm aerosol dynamics. *Atmos. Meas. Technol.* **10**, 1639–1651 (2017).
180. Jiang, J. K., Chen, M. D., Kuang, C. A., Attoui, M. & McMurry, P. H. Electrical mobility spectrometer using a diethylene glycol condensation particle counter for measurement of aerosol size distributions down to 1 nm. *Aerosol Sci. Technol.* **45**, 510–521 (2011).
181. Kangasluoma, J. et al. Heterogeneous nucleation onto ions and neutralized ions: insights into sign-preference. *J. Phys. Chem. C.* **120**, 7444–7450 (2016).
182. Kangasluoma, J. et al. Sub-3 nm particle size and composition dependent response of a nano-CPC battery. *Atmos. Meas. Technol.* **7**, 689–700 (2014).
183. Winkler, P. M. et al. Heterogeneous nucleation experiments bridging the scale from molecular ion clusters to nanoparticles. *Science* **319**, 1374–1377 (2008).
184. Kupc, A. et al. Laboratory characterization of a new nano-water-based CPC 3788 and performance comparison to an ultrafine butanol-based CPC 3776. *Aerosol Sci. Technol.* **47**, 183–191 (2013).
185. Kulmala, M. et al. The condensation particle counter battery (CPCB): a new tool to investigate the activation properties of nanoparticles. *J. Aerosol Sci.* **38**, 289–304 (2007).
186. Kangasluoma, J. & Kontkanen, J. On the sources of uncertainty in the sub-3 nm particle concentration measurement. *J. Aerosol Sci.* **112**, 34–51 (2017).
187. Wimmer, D. et al. Technical note: using DEG-CPCs at upper tropospheric temperatures. *Atmos. Chem. Phys.* **15**, 7547–7555 (2015).
188. Gormley, P. G. & Kennedy, M. Diffusion from a stream flowing through a cylindrical tube. *Proc. R. Ir. Acad. A Math. Phys. Sci.* **52**, 163–169 (1949).
189. Kangasluoma, J. et al. Operation of the Airmodus A11 nano Condensation Nucleus Counter at various inlet pressures and various operation temperatures, and design of a new inlet system. *Atmos. Meas. Technol.* **9**, 2977–2988 (2016).
190. Fu, Y., Xue, M., Cai, R., Kangasluoma, J. & Jiang, J. Theoretical and experimental analysis of the core sampling method: reducing diffusional losses in aerosol sampling line. *Aerosol Sci. Technol.* **53**, 793–801 (2019).
191. Seinfeld, J. H. & Pandis, S. N. *Atmospheric Chemistry and Physics: From Air Pollution to Climate Change* (Wiley, 2012).
192. Poling, B. E., Prausnitz, J. M. & O'Connell, J. P. *The Properties of Gases and Liquids* 5 (McGraw-Hill, 2001).
193. Seinfeld, J. H. & Pandis, S. *Atmospheric Chemistry and Physics: From Air Pollution to Climate Change*, 3rd edn (Wiley, 2016).
194. Mikkonen, S. et al. Technical note: effects of uncertainties and number of data points on line fitting—a case study on new particle formation. *Atmos. Chem. Phys.* **19**, 12531–12543 (2019).
195. Press, W. H., Flannery, B. P., Teukolsky, S. & Vettering, W. T. *Numerical Recipes—The Art of Scientific Computing* (Cambridge University Press, 1986).
196. Tellinghuisen, A. Monte Carlo study of precision, bias, inconsistency, and non-gaussian distributions in nonlinear least squares. *J. Phys. Chem. A* **104**, 2834–2844 (2000).
197. Manninen, H. E. et al. Long-term field measurements of charged and neutral clusters using neutral cluster and air ion spectrometer (NAIS). *Boreal Environ. Res.* **14**, 591–605 (2009).
198. Bates, D. in *Advances in Atomic and Molecular Physics* Vol. 20 1–40 (Elsevier, 1985).

199. Franchin, A. et al. Experimental investigation of ion-ion recombination under atmospheric conditions. *Atmos. Chem. Phys.* **15**, 7203–7216 (2015).
200. Hoppel, W. A. & Frick, G. M. Ion aerosol attachment coefficients and the steady-state charge-distribution on aerosols in a bipolar ion environment. *Aerosol Sci. Technol.* **5**, 1–21 (1986).
201. Hering, S. V., Stolzenburg, M. R., Quant, F. R., Oberreit, D. R. & Keady, P. B. A laminar-flow, water-based condensation particle counter (WCPC). *Aerosol Sci. Technol.* **39**, 659–672 (2005).
202. Mirme, A. et al. A wide-range multi-channel air ion spectrometer. *Boreal Environ. Res.* **12**, 247–264 (2007).
203. Kürten, A. et al. Neutral molecular cluster formation of sulfuric acid-dimethylamine observed in real time under atmospheric conditions. *Proc. Natl Acad. Sci. USA* **111**, 15019–15024 (2014).
204. Tiszenkel, L. et al. Temperature effects on sulfuric acid aerosol nucleation and growth: initial results from the TANGENT study. *Atmos. Chem. Phys.* **19**, 8915–8929 (2019).
205. Benson, D. R., Erupe, M. E. & Lee, S.-H. Laboratory-measured H_2SO_4-H_2O-NH_3 ternary homogeneous nucleation rates: initial observations. *Geophys. Res. Lett.* **36**, L15818 (2009).
206. Erupe, M. E., Viggiano, A. A. & Lee, S. H. The effect of trimethylamine on atmospheric nucleation involving H_2SO_4. *Atmos. Chem. Phys.* **11**, 4767–4775 (2011).
207. Krasnomowitz, J. M. et al. Growth of Aitken mode ammonium sulfate particles by α-pinene ozonolysis. *Aerosol Sci. Technol.* **53**, 406–418 (2019).
208. Stangl, C. M. et al. Sulfur dioxide modifies aerosol particle formation and growth by ozonolysis of monoterpenes and isoprene. *J. Geophys. Res. Atmos.* **124**, 4800–4811 (2019).

Acknowledgements

The CLOUD community is gratefully acknowledged for invaluable discussions. Partial funding was provided by the Academy of Finland (project nos. 316114 and 325647). The work was also supported by the Academy of Finland via the BioFuture2025 project 'Nano BioMass', an Academy professor project of M.K. and the Center of Excellence in Atmospheric Sciences (project no. 307331), the European Commission via ACTRIS2 (project no. 654109) and the European Research Council via advanced grant ATM-GTP (project no. 742206).

Author contributions

L.D., K. Lehtipalo, J. Kontkanen, T.N., K. Lehtinen, V.-M.K. and M.K. contributed to the development of the technique for calculating J_{dp} and GR. R.B., L.A., J.D., T.P., C.Y., B.C. and J. Kangasluoma contributed to development of the technique for calibrating and minimizing losses during particle measurement. All authors contributed to the writing of this protocol and to the scientific discussions related to it.

Competing interests

The authors declare no competing interests.

Additional information

Supplementary information is available for this paper at https://doi.org/10.1038/s41596-019-0274-z.

Correspondence and requests for materials should be addressed to M.K. or J.K.

Peer review information *Nature Protocols* thanks Véronique Riffault and the other, anonymous, reviewer(s) for their contribution to the peer review of this work.

Received: 1 April 2019; Accepted: 27 November 2019;
Published online: 12 February 2020

Related links

Key references using this protocol

Lehtipalo, K. et al. *Sci. Adv.* **4**, eaau5363 (2018): https://doi.org/10.1126/sciadv.aau5363

Wagner, R. et al. *Atmos. Chem. Phys.* **17**, 15181–15197 (2017): https://doi.org/10.5194/acp-17-15181-2017 natureresearch

Corresponding author(s): Lubna Dada, Markku Kulmala, Juha Kangasluoma

Last updated by author(s): Apr 2, 2019

Reporting Summary

Nature Research wishes to improve the reproducibility of the work that we publish. This form provides structure for consistency and transparency in reporting. For further information on Nature Research policies, see Authors & Referees and the Editorial Policy Checklist.

Statistics

For all statistical analyses, confirm that the following items are present in the figure legend, table legend, main text, or Methods section.

n/a	Confirmed	
☒	☐	The exact sample size (n) for each experimental group/condition, given as a discrete number and unit of measurement
☒	☐	A statement on whether measurements were taken from distinct samples or whether the same sample was measured repeatedly
☒	☐	The statistical test(s) used AND whether they are one- or two-sided *Only common tests should be described solely by name; describe more complex techniques in the Methods section.*
☒	☐	A description of all covariates tested
☒	☐	A description of any assumptions or corrections, such as tests of normality and adjustment for multiple comparisons
☒	☐	A full description of the statistical parameters including central tendency (e.g. means) or other basic estimates (e.g. regression coefficient) AND variation (e.g. standard deviation) or associated estimates of uncertainty (e.g. confidence intervals)
☒	☐	For null hypothesis testing, the test statistic (e.g. F, t, r) with confidence intervals, effect sizes, degrees of freedom and P value noted *Give P values as exact values whenever suitable.*
☒	☐	For Bayesian analysis, information on the choice of priors and Markov chain Monte Carlo settings
☒	☐	For hierarchical and complex designs, identification of the appropriate level for tests and full reporting of outcomes
☒	☐	Estimates of effect sizes (e.g. Cohen's d, Pearson's r), indicating how they were calculated

Our web collection on statistics for biologists contains articles on many of the points above.

Software and code

Policy information about availability of computer code

Data collection	A method is provided in the protocol with anticipated data.
Data analysis	MATLAB

For manuscripts utilizing custom algorithms or software that are central to the research but not yet described in published literature, software must be made available to editors/reviewers. We strongly encourage code deposition in a community repository (e.g. GitHub). See the Nature Research guidelines for submitting code & software for further information.

Data

Policy information about availability of data

All manuscripts must include a data availability statement. This statement should provide the following information, where applicable:

- Accession codes, unique identifiers, or web links for publicly available datasets
- A list of figures that have associated raw data
- A description of any restrictions on data availability

The data used in the figures can be provided upon request from the corresponding authors.

Field-specific reporting

Please select the one below that is the best fit for your research. If you are not sure, read the appropriate sections before making your selection.

☐ Life sciences ☐ Behavioural & social sciences ☒ Ecological, evolutionary & environmental sciences

For a reference copy of the document with all sections, see nature.com/documents/nr-reporting-summary-flat.pdf

Ecological, evolutionary & environmental sciences study design

All studies must disclose on these points even when the disclosure is negative.

Study description	The protocol provides a procedure for calculating particle formation and growth rates from chamber experiments.
Research sample	No samples are used.
Sampling strategy	N/A
Data collection	N/A
Timing and spatial scale	N/A
Data exclusions	N/A
Reproducibility	N/A
Randomization	N/A
Blinding	N/A

Did the study involve field work? ☐ Yes ☒ No

Reporting for specific materials, systems and methods

We require information from authors about some types of materials, experimental systems and methods used in many studies. Here, indicate whether each material, system or method listed is relevant to your study. If you are not sure if a list item applies to your research, read the appropriate section before selecting a response.

Materials & experimental systems

n/a	Involved in the study
☒	☐ Antibodies
☒	☐ Eukaryotic cell lines
☒	☐ Palaeontology
☒	☐ Animals and other organisms
☒	☐ Human research participants
☒	☐ Clinical data

Methods

n/a	Involved in the study
☒	☐ ChIP-seq
☒	☐ Flow cytometry
☒	☐ MRI-based neuroimaging